Measurement of the Two Neutrino Double Beta Decay Half-life of ^{150}Nd with the NEMO-3 Detector

A dissertation submitted to the University of Manchester for the degree of Master of Science
in the Faculty of Engineering and Physical Sciences

2011

Kiyotaka Yamazaki

Particle Physics Group
School of Physics and Astronomy

Contents

List of Figures

List of Tables

Abstract

Using 36.55 g of ^{150}Nd sample and 1648 days of data taken by the NEMO-3 experiment, the two neutrino double beta decay half-life of ^{150}Nd is measured to be

$$T_{1/2}^{2\nu} = \left(8.95^{+0.28}_{-0.26}(\text{stat}) \pm 0.50(\text{sys})\right) \times 10^{18}\text{years}$$

A study of the background events and the application of a laser calibration system of energy measurements was made.

Declaration

No portion of the work referred to in the thesis has been submitted in support of an application for another degree or qualification of this or any other university or other institute of learning.

Copyright Statement

Acknowledgements

First and foremost I would like to thank my supervisor Stefan Söldner-Rembold for his guidance, patience and support over the past thirteen months. His wide knowledge and encouragement have been of great value for me.
I would also like to thank Chris Jackson. This dissertation would not have been possible without his great amount of assistance and advice.
I am grateful to Stefano Torre for the generation of MC and his help with computing and all the members of NEMO-3 for detailed and constructive comments on my work. Thanks to Will Poynter for his computing help while I am away from England, and to Manu Chauveau for the proof reading.
Thanks to Fred Loebinger for giving me this wonderful opportunity and a lot of help, and to all the members of the Manchester Particle Physics group who made my time as a postgraduate student so special and enjoyable. Thanks to Ching-Hung Lai for his assistance on submitting the dissertation.
And last but not least, I would like to thank my family for their continuous support.

Statement of Work Completed

The author measured the activities of internal backgrounds of ^{150}Nd foil using the background model constructed by the previous studies. The work is presented in Chapter 4.

The author also measured the activity of ^{150}Nd including the optimization of the event selection criteria and the use of the Laser Energy Corrections which is presented in Chapter 5

Chapter 1

Theoretical Background

1.1 Introduction

In 1930, W. Pauli proposed a neutral, massless particle, the "*neutron*", in order to explain the continuous energy spectrum of β decay [1]. Four years later, E. Fermi renamed the "*neutron*" to "*neutrino*" and published a successful model of β decay, later known as Fermi coupling [2]. Since then, the neutrino has been recognized as one of the fundamental particles of the Standard Model (SM). However, many open questions still remain. For example, the number of neutrino species, the absolute mass of the neutrino, the Dirac/Majorana nature and the parameters of the Pontecorvo-Maki-Nakagawa-Sakata (PMNS) matrix are all yet to be determined. Recently (June 2011) an indication of non-zero θ_{13}, which is the last unmeasured mixing angle of the PMNS matrix, has been observed [3]. Therefore, neutrino physics is one of the most interesting topics in Particle Physics.

The observation of neutrinoless double β decay ($0\nu\beta\beta$) will help to answer

some of the remaining questions such as the Dirac/Majorana nature of neutrinos, the absolute mass scale and the hierarchy of neutrino mass eigenstates. Exploring these questions will have important implications for modern physics. The measurement of two neutrino double β decay ($2\nu\beta\beta$) is important not only for studying nuclear matrix elements (NME) but also to search for $0\nu\beta\beta$ decays as it is an important background for this beyond the Standard Model (BSM) process. NEMO-3 was one of the experiments aiming to investigate these processes with a sensitivity for measuring half-lives of $\approx 10^{24}$ years [4].

1.2 The Standard Model and Neutrino

The SM of particle physics is a theory of interactions between the fundamental particles, which is symmetric under a gauge transformation of $SU_C(3) \times SU_L(2) \times U_Y(1)$. In the SM, the weak bosons and the charged leptons gain their mass through the Higgs mechanism. Neutrinos were believed to be massless and only left-handed neutrinos and right-handed anti-neutrinos were experimentally observed. However, the neutrino oscillations observed by experiments such as the Homestake Solar Neutrino Observatory [5], SNO+ [6] and SuperKamiokande [7] implies non-zero neutrino mass. Neutrinos do not have a Higgs term in the SM. They are assumed to acquire mass not by the Higgs mechanism but by a different mechanism.

1.3 The Nature and Mass of Neutrino

As neutrinos are electrically neutral, they can be either Dirac or Majorana particles. Dirac particles are defined such that the particles are distinct from their anti-particles, i.e.,

$$C|\psi_D\rangle = |\overline{\psi_D}\rangle \text{ with } |\psi_D\rangle \neq |\overline{\psi_D}\rangle, \tag{1.1}$$

where ψ_D is the wave function of a Dirac particle and $\overline{\psi_D}$ is the wave function of its anti-particle and C is the charge conjugation operator. Majorana particles are the anti-particles of themselves, i.e.,

$$C|\psi_M\rangle = |\psi_M\rangle, \tag{1.2}$$

where ψ_M is the wave function of a Majorana particle. Thus, it implies lepton number violation. In the SM Lagrangian, the Dirac mass term mixes the left- and right-handed components,

$$\mathcal{L}_D = m_D \left(\overline{\psi_L}\psi_R + \overline{\psi_R}\psi_L\right). \tag{1.3}$$

The Majonara mass terms of the right-handed and the left-handed neutrinos are written as

$$\mathcal{L}_M^R = \frac{1}{2} m_M^R \left(\overline{\psi_L^C}\psi_R + \overline{\psi_R}\psi_L^C\right), \tag{1.4}$$

$$\mathcal{L}_M^L = \frac{1}{2} m_M^L \left(\overline{\psi_L}\psi_R^C + \overline{\psi_R^C}\psi_L\right), \tag{1.5}$$

respectively, where ψ^C is a charge conjugate of ψ. One of the models for neutrinos to acquire mass is the see-saw mechanism. It includes both the Dirac and the Majorana mass terms and is expressed as

$$\mathcal{L}_{see-saw} = \mathcal{L}_D + \mathcal{L}_M = \frac{1}{2}\begin{pmatrix}\overline{\psi_L} & \overline{\psi_L^C}\end{pmatrix} \cdot \mathcal{M}_{DM} \cdot \begin{pmatrix}\psi_R^C \\ \psi_R\end{pmatrix} + h.c., \tag{1.6}$$

where $h.c.$ is the Hermitian conjugate and $\mathcal{M}_{DM}$ is the mass matrix

$$\mathcal{M}_{DM} = \begin{pmatrix} m_M^L & m_D \\ m_D & m_M^R \end{pmatrix}. \tag{1.7}$$

Usually, m_M^L, m_M^R and m_D are assumed to be zero, of order of the Grand Unified Theory (GUT) scale ($\approx 10^{15}$ GeV) and of order of the electroweak scale ($\approx$100 GeV), respectively. By diagonalizing the matrix, the mass eigenstates

$$\Psi_{heavy} = \left(\psi_R + \psi_R^C\right) - \frac{m_D}{m_M^R}\left(\psi_L + \psi_L^C\right) \tag{1.8}$$

$$\Psi_{light} = \left(\psi_L + \psi_L^C\right) + \frac{m_D}{m_M^R}\left(\psi_R + \psi_R^C\right) \tag{1.9}$$

are obtained. The heavy mass eigenvalue is calculated to be $\approx m_M^R$ ($\approx 10^{15}$ GeV) and the light one is $\approx m_D^2/m_M^R$ ($\approx$0.01 eV). The see-saw mechanism explains the smallness of the mass of the light neutrino (which is mainly composed of the left-handed states) compared to the other SM particles. It suggests that the heavy neutrino (which is mainly composed of the right-handed states) has decayed in the early Universe and has therefore not been observed so far.

1.4 PMNS matrix

As with quarks, the mass eigenstates of the neutrinos are different from their weak eigenstates. The relation between them is described by the PMNS matrix

$$\begin{pmatrix} \nu_e \\ \nu_\mu \\ \nu_\tau \end{pmatrix} = \begin{pmatrix} U_{e1} & U_{e2} & U_{e3} \\ U_{\mu 1} & U_{\mu 2} & U_{\mu 3} \\ U_{\tau 1} & U_{\tau 2} & U_{\tau 3} \end{pmatrix} \begin{pmatrix} \nu_1 \\ \nu_2 \\ \nu_3 \end{pmatrix}. \tag{1.10}$$

Since the PMNS matrix is unitary, it can be written in terms of the mixing angles and the Dirac phase (which indicates the CP-violation),

$$U_{\alpha i} = \begin{pmatrix} c_{12} & s_{12} & 0 \\ -s_{12} & c_{12} & 0 \\ 0 & 0 & 1 \end{pmatrix} \begin{pmatrix} 1 & 0 & 0 \\ 0 & c_{23} & s_{23} \\ 0 & -s_{23} & c_{23} \end{pmatrix} \begin{pmatrix} c_{13} & 0 & s_{13}e^{-i\delta} \\ 0 & 1 & 0 \\ -s_{13}e^{i\delta} & 0 & c_{13} \end{pmatrix} D, \quad (1.11)$$

where c_{ij} and s_{ij} are the cosine and the sine of the mixing angle θ_{ij} and D is a diagonal matrix containing Majorana phase angles ϕ,

$$D = \begin{pmatrix} 1 & 0 & 0 \\ 0 & e^{\phi_1} & 0 \\ 0 & 0 & e^{\phi_2} \end{pmatrix}. \quad (1.12)$$

D only appears if the neutrinos are Majorana particles. The angle θ_{12} was measured by solar neutrino experiments [8] and θ_{23} was measured by atmospheric neutrino experiments [9]. The angle θ_{13} is currently being measured by experiments such as the T2K [3] and MINOS [10] experiments.

1.5 Double Beta Decay

1.5.1 Two Neutrino Double Beta Decay

The two neutrino double β decay is a SM process that is described by

$$(A, Z) \rightarrow (A, Z+2) + 2e^- + 2\overline{\nu_e}, \quad (1.13)$$

where A is the mass number and Z is the atomic number (Fig. 1.1a). This decay takes place in nuclei for which a single β decay is forbidden or strongly suppressed due to energy conservation (or angular momentum conservation) as shown in Fig. 1.2. In this process, all the quantum numbers including

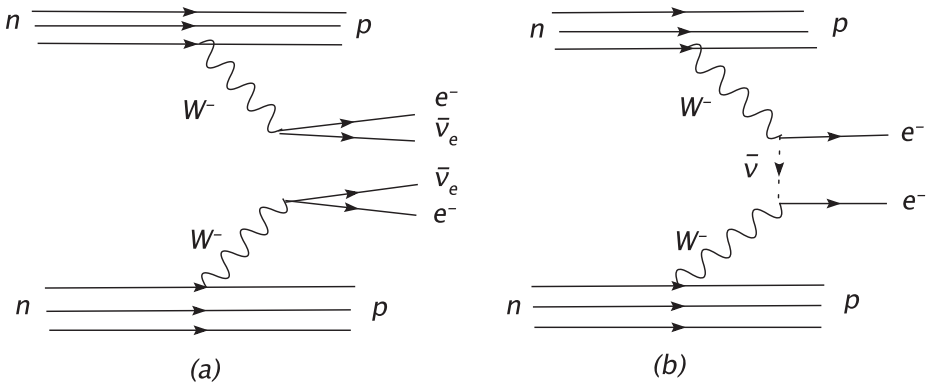

Figure 1.1: Diagrams of (a) $2\nu\beta\beta$ and (b) $0\nu\beta\beta$ decays.

lepton number are conserved unlike $0\nu\beta\beta$ (Fig. 1.1b), hence it is allowed by the standard electroweak theory. The associated nuclear transition energy $Q_{\beta\beta}$ is defined as

$$Q_{\beta\beta} = m(A, Z) - m(A, Z + 2) - 2m_e, \tag{1.14}$$

where $m(A, Z)$, $m(A, Z + 2)$ and m_e are the mass of the mother nucleus, the daughter nucleus and the electron, respectively. The half-life, $T^{2\nu}_{1/2}$, of this process is written as

$$\frac{1}{T^{2\nu}_{1/2}} = G^{2\nu} \left| \mathfrak{M}^{2\nu} \right|^2, \tag{1.15}$$

where $G^{2\nu}$ is a phase space factor and $\mathfrak{M}^{2\nu}$ is a nuclear matrix element (NME). Both $G^{2\nu}$ and $\mathfrak{M}^{2\nu}$ are calculable, but $\mathfrak{M}^{2\nu}$ is model dependent. Therefore, it is vital to extract the value of $\mathfrak{M}^{2\nu}$ experimentally [11].

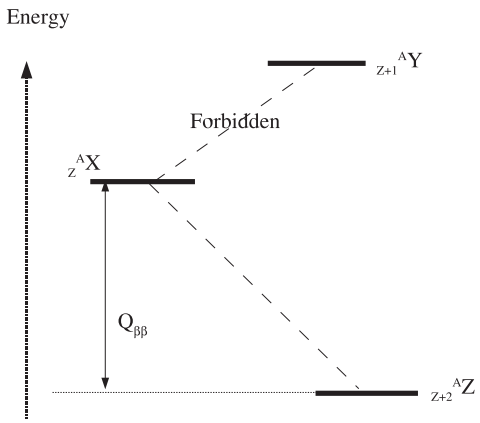

Figure 1.2: A schematic energy diagram for double β decay isotope X. A decay to isotope Y is energetically forbidden while a decay to isotope Z is favoured.

Chapter 2

The NEMO-3 Experiment

2.1 NEMO-3 Detector

There are several types of double β decay experiments: homogeneous and heterogeneous. For the homogeneous experiments, such as semiconductor calorimeters or Xe time projection chambers (TPCs), the source and the detector are identical and the choice of the isotope is not flexible. For the heterogeneous experiments such as NEMO-3, which has a source foil in between tracker and calorimeter, flexibility in the choice of isotopes is given. This feature allowed the NEMO-3 to study double β decay half-lives for several isotopes.

The NEMO-3, shown schematically in Fig. 2.1, was a cylindrical detector that was located at LSM Modane, France, where the depth is 4800 meters water equivalent (m.w.e.). This provided a low cosmic ray background as shown in Fig. 2.2 [12]. There were 7 different $\beta\beta$ isotopes with a total mass of $\approx$ 10 kg and a tracker with 6180 drift cells to identify the tracks of the particles. At the walls of the detector, there were 1940 plastic scintillators

coupled to low-radioactive photomultiplier tubes (PMTs). A solenoid provided a magnetic field designed to be 25 Gauss and orientated vertically through the detector. The whole setup was covered with pure iron and water and wood to shield from photons and neutrons outside the detector.

2.2 Double Beta Decay Isotopes in NEMO-3

Isotope	Mass	$Q_{\beta\beta}$ (keV)
^{100}Mo	6.914 kg	3034
^{82}Se	0.932 kg	2995
^{116}Cd	405 g	2805
^{96}Zr	9.4 g	3350
^{150}Nd	36.6 g	3367
^{48}Ca	7.0 g	4272
^{130}Te	454 g	2529

Table 2.1: $\beta\beta$ isotopes in NEMO-3 [13].

Table 2.1 shows the double β decay isotopes in the detector. They were chosen because of the high $Q_{\beta\beta}$-value so that the $\beta\beta$ signals can be easily isolated from low Q-value backgrounds [4]. Since $2\nu\beta\beta$ decay is a rare process, these choices are important to gain better signal to background ratios. As well as measuring $2\nu\beta\beta$ half-lives of all these isotopes, the experiment was particularly designed to search for $0\nu\beta\beta$ decays of ^{100}Mo and ^{82}Se with higher mass. The source foils are placed in the detector as shown in Fig. 2.3.

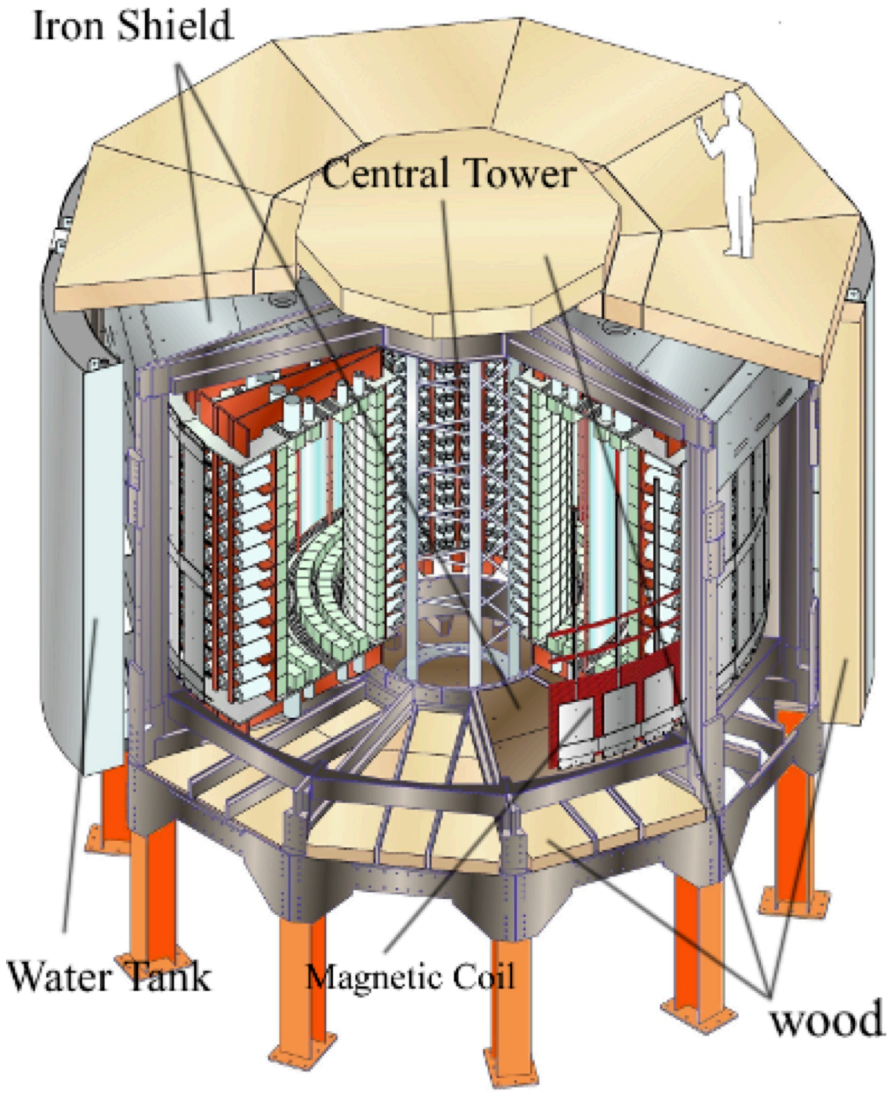

Figure 2.1: Design of the NEMO-3 detector [13].

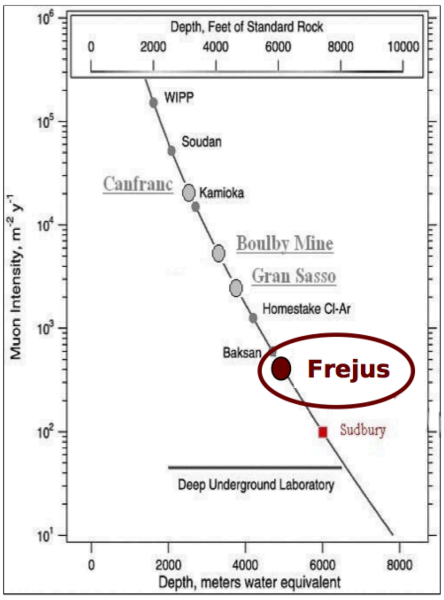

Figure 2.2: The intensity of muon background at Frejus, Modane [12].

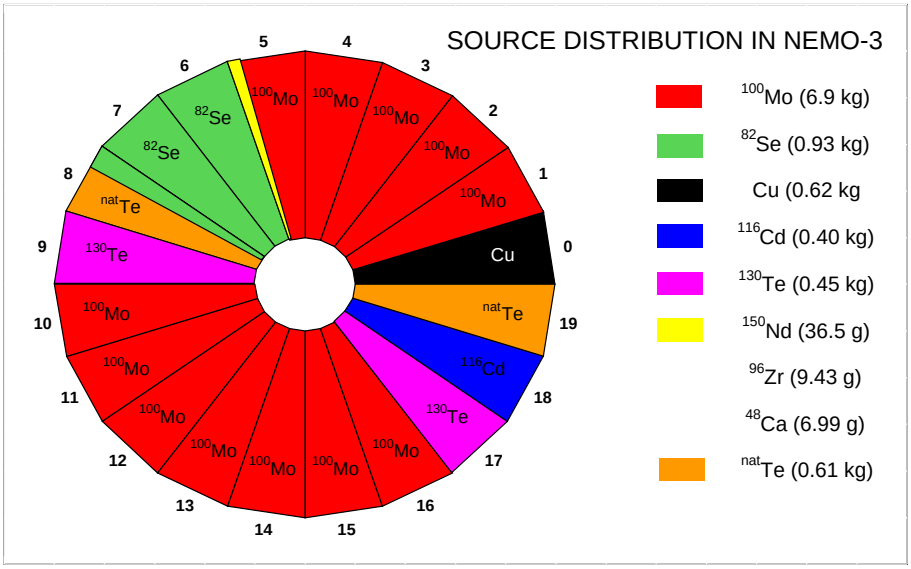

Figure 2.3: The distribution of the isotopes throughout the 20 sectors of the NEMO-3 detector [13].

2.2.1 ^{150}Nd Isotope

In this dissertation, decays of Neodymium-150 (^{150}Nd) are studied. ^{150}Nd undergoes $2\nu\beta\beta$ decay to ^{150}Sm. It predominantly decays to the ground state, but it can also decay to the 0_1^+ and the 2_1^+ excited states. The excited ^{150}Sm nucleus emits photon(s) with the energy shown in the decay scheme in Fig. 2.4. Due to its high $Q_{\beta\beta}$-value (Tab. 2.1) and the high atomic number, ^{150}Nd has the largest phase space factor of all the $\beta\beta$ isotopes. However, deformation of the nucleus leads to a large uncertainty in the calculation of the NME for this isotope [14]. Thus the theoretical uncertainty on the neutrino mass calculation is large.

The ^{150}Nd foil for the NEMO-3 was produced in the Institute for Nuclear Research of Moscow, Russia. After several purification processes, the foil is enriched with 36.55 ± 0.10 g of ^{150}Nd. Together with a Mylar support foil (6.458 g) and some impurities, its mass is 57 g in total. The impurities were identified to be ^{207}Bi, ^{214}Bi, ^{152}Eu, ^{214}Pb, ^{234m}Pa, ^{208}Tl and ^{40}K by using a high purity germanium (HPGe) detector [13]. In the detector, the ^{150}Nd foil is located in Sector 5 as shown in Fig. 2.3. The geometry of the foil was defined as

$$1.802 < \phi < 1.845 \text{ rad}, \tag{2.1}$$

$$-117.0 < z < 117.0 \text{ cm}, \tag{2.2}$$

using the cylindrical coordinate system of the detector [4].

2.3 Tracker

The NEMO-3 tracks charged particles by drift cells operating in Geiger mode. Each sector contains 9 layers of 30 mm diameter cells on the inner and outer

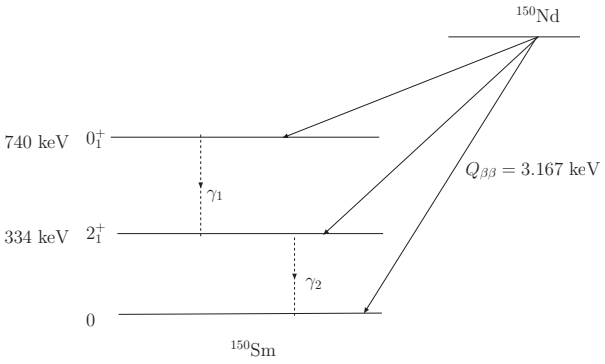

Figure 2.4: An energy diagram showing a decay of ^{150}Nd to ^{150}Sm [15].

side and they are arranged as a pattern of 4-2-3 layers (Fig. 2.5). It is filled with a gas of helium (95%), ethanol (4%), argon (1%) and water (1500 ppm). When a charged particle passes through the gas, it ionizes He atoms and the ionized electrons drifted towards the anode wire causing further ionizations. The avalanche of ionization makes a measurable pulse when it reached the wire and plasma propagates along wire to cathode rings at both ends of the wire (Fig. 2.6). A time to digital converter (TDC) attached at the end of the anode wire measured the arrival time of the signal to determine the transverse position of the hit. Helium is the lowest atomic number noble gas, therefore it causes minimum energy loss of the charged particles and remains stable inside the detector. Alcohol molecules were used to quench the avalanche of the electrons. Argon and water were added in order to improve the quality of the signal by increasing the plasma propagation efficiency and reducing the noise.

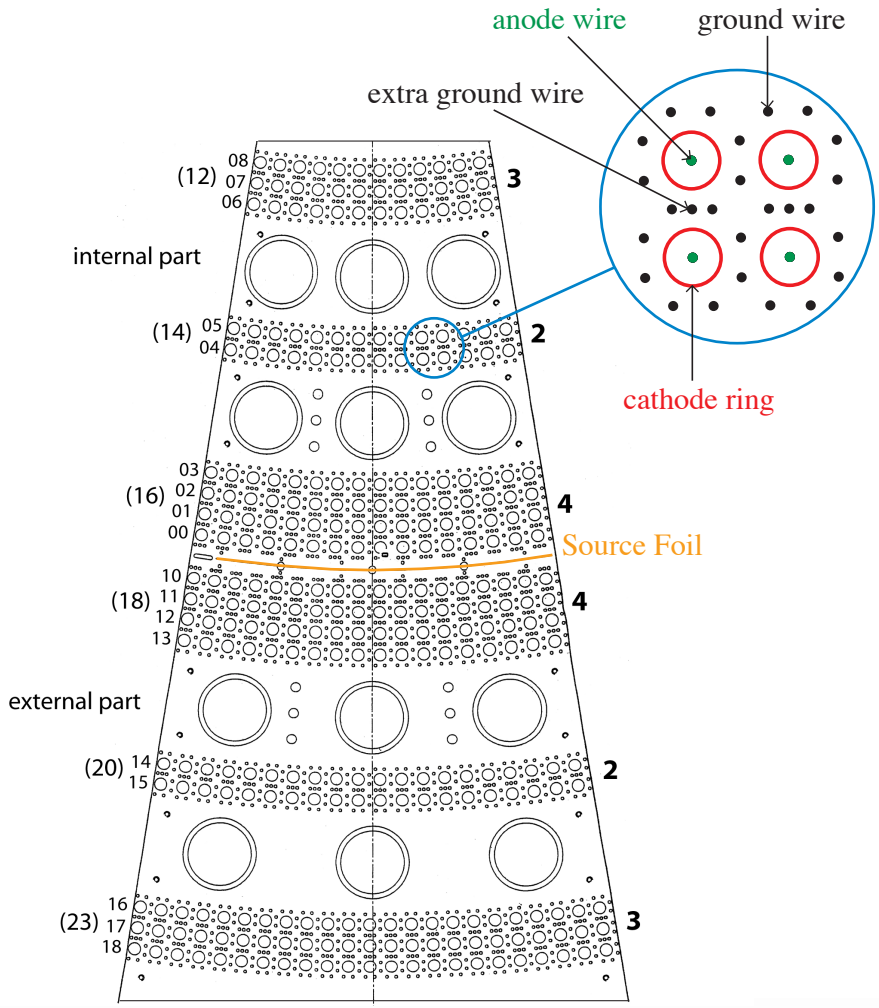

Figure 2.5: A top view of a sector of the NEMO-3 detector. The 4-2-3 configuration of the drift cell layers and the PMTs on the top and bottom are shown [13].

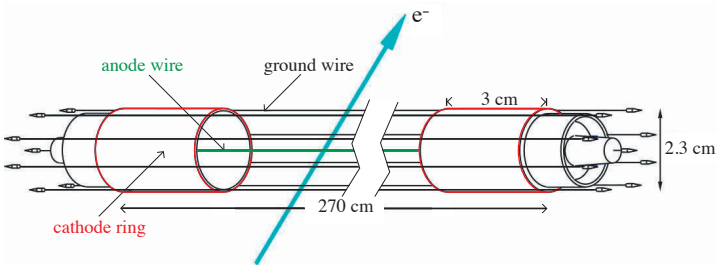

Figure 2.6: A drift cell of the detector [13]. As an electron passes through, the gas is ionized and the signal is picked up by the cathode ring at the end.

2.4 Measuring the Energy of the Particles

The NEMO-3 measured energies of particles with calorimeters, which consisted of scintillators and PMTs (Sec. 2.4.1). The calorimeters were calibrated by two methods: absolute energy calibration (Sec. 2.4.2) and Laser calibration (Sec. 2.4.3 and Sec. 2.4.4). The absolute energy calibration was performed approximately six times a year and the laser calibration was realized during every interval between the normal runs.

2.4.1 Scintillators and PMTs

The scintillators and PMTs were installed to measure the energy of the particles. Fig. 2.7 illustrates the calorimeter layout. The scintillators were made of polystyrene. When a charged particle passes through the scintillator, the energy is absorbed by the polystyrene molecules and the excited molecules

emit photons to de-excite. A photon loses its energy via Compton scattering and the scattered electron loses the energy as described before. The PMTs multiply the photons produced by the scintillator to measurable level of electrical signals by the avalanche of the photoelectric effect.
There are two sizes of radio-pure PMTs, 3" and 5", both capable of measuring the energy range from 0 to 12 MeV [4]. The 3" PMTs are mounted on the inner wall of the calorimeter and the 5" PMTs are mounted on the outer wall (Fig. 2.8). The top and the bottom of the detector are attached with both 3" and 5" PMTs. The signals from PMTs are also used to measure TOFs and charge integrations with TDCs and analogue to digital converters (ADCs).

2.4.2 Absolute Energy Calibration

The calorimeters were calibrated with ^{207}Bi and ^{90}Sr sources of known activities for periods of $\approx$ 72 hours. The ^{207}Bi source provides two peaks of 482 keV and 976 keV electron energies via a conversion process of γ decay. The higher energy region (above 1.5 MeV) was calibrated by a measurement of the energy spectrum of the daughter isotope of ^{90}Sr, ^{90}Y. This is a pure β emitter and has an end point energy of 2283 keV. The results of the ^{207}Bi and the ^{90}Y energy measurements were combined to calculate a linear response of each PMT that is valid for the energy region up to 4 MeV [13].

2.4.3 Laser Energy Correction

Calibration of the calorimeters was also performed by shining lasers on PMTs. A laser light of known energy was sent directly to the PMTs via optical fibers.

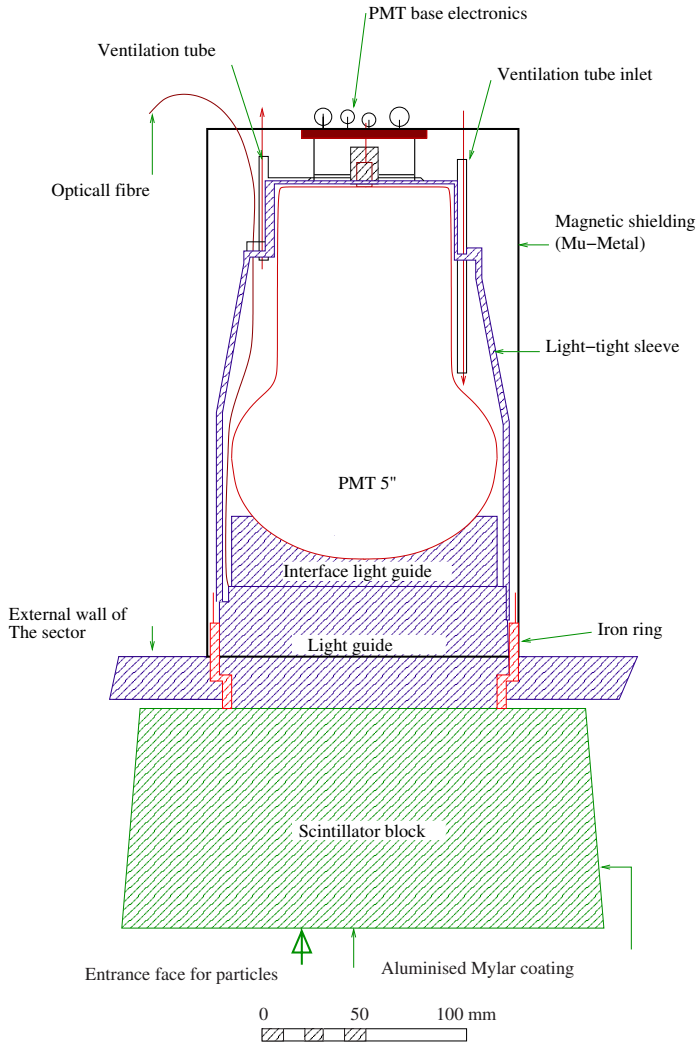

Figure 2.7: A schematic diagram of an external calorimeter block [4]. A PMT is attached to a scintillator block with a light guide.

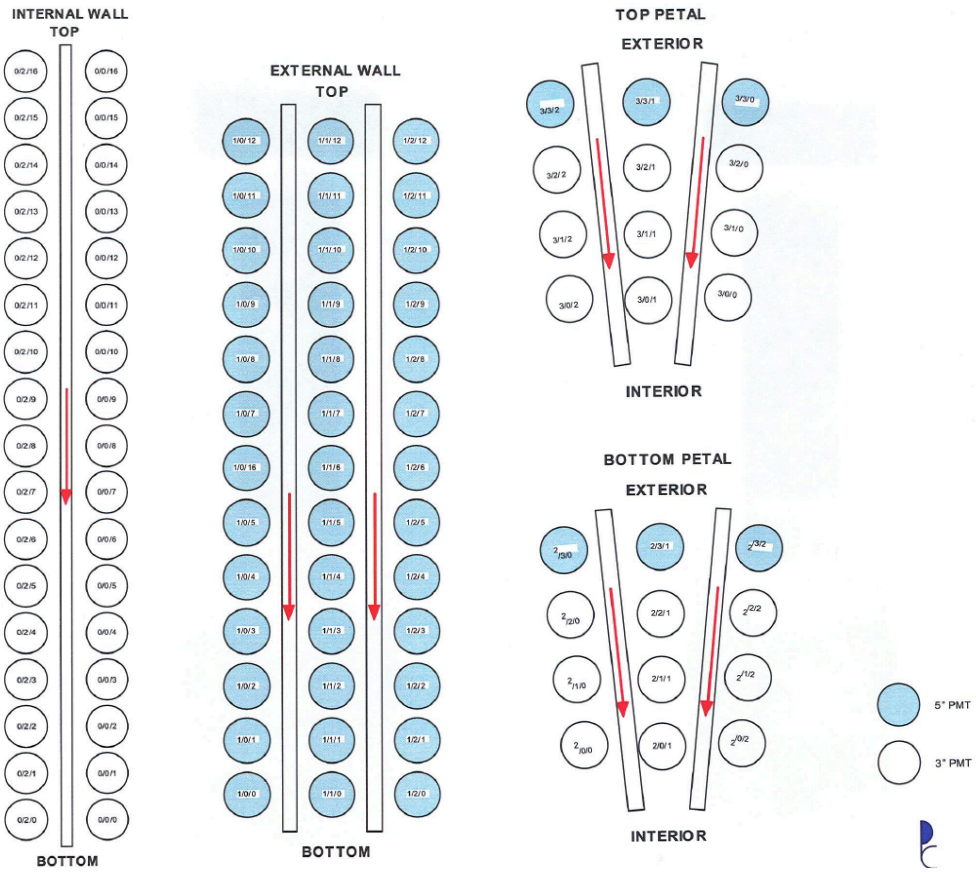

Figure 2.8: Alignment of PMTs on each wall [13].

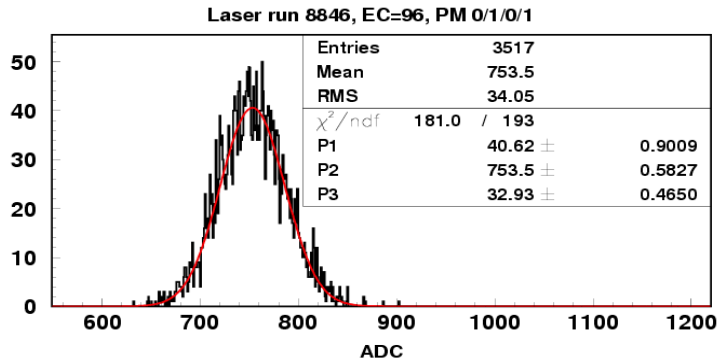

Figure 2.9: An example of an ADC distribution and Gaussian fit [16].

The ADC charge distribution was measured for each PMTs.

A Gaussian distribution was fitted and the corresponding χ^2_{ADC} value was calculated (Fig. 2.9). The energy of the incident beam, E_I, was calculated for each PMT in every laser run and the ratio

$$R = \frac{E_I}{E_R} \tag{2.3}$$

was obtained, where E_R is defined as the value in the reference run chosen at the middle of the absolute energy calibration with the ^{207}Bi source. The beam energy generally decreased with time. In order to take this into account, the variation V was calculated by

$$V = \frac{\langle E_I \rangle}{\langle E_R \rangle}. \tag{2.4}$$

The mean values were obtained from the mean of all the stable PMTs. The correction coefficient (LEC value) is defined as

$$\text{LEC value} = \frac{R}{V}. \tag{2.5}$$

The correction values are stored in the NEMO-3 database and the variation is recorded. A linear fit is done to the variation plot (Fig. 2.10) and the corresponding χ^2_{linear} is determined.

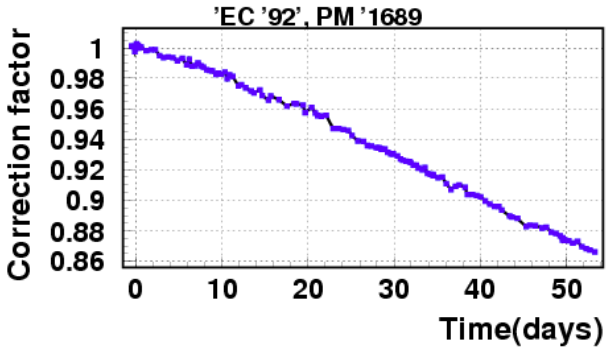

(a)

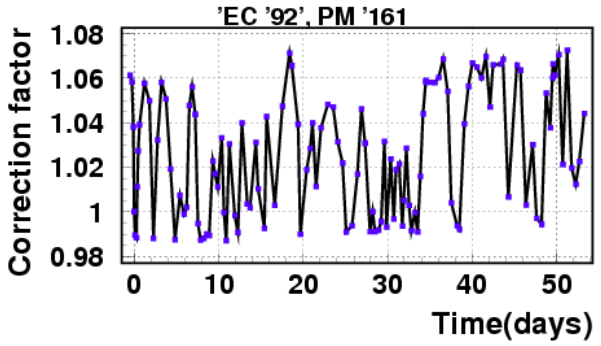

(b)

Figure 2.10: Examples of (a) a linear distribution of LEC value and (b) a non-linear distribution of LEC value [16].

In addition, LEC quality flag was defined as the following in order to determine the stability of the PMTs.

- +1: bad laser ADC distribution e.g. $\chi^2_{ADC} > 2.5$;
- +2: bad linear fit through corrections e.g. $\chi^2_{linear} > 10$;
- +4: maximum correction value > 4 % during the survey period;
- +8: amplitude of correction value > 5 %.

The measured energy was divided by the LEC value to get the corrected energy. For some PMTs in some runs, an LEC was not available due to reasons such as:

- no laser light was available;
- too few counts in ADC distribution;
- laser light energy was too low;
- the gain was too low.

2.4.4 Laser Time Correction

The TDCs were calibrated with laser. During the laser run j, a correction factor, LTC, was calculated by

$$LTC^i_j = tdc^i_j - tdc^i_{reference}, \tag{2.6}$$

where tdc^i is the time measured by the PMT i. The run number 1404 was chosen as the reference run because of its relative stability compared to other

runs [17]. Hence, tdc of the data, which was taken during the k-th run that is the nearest to the laser run j, is corrected as following,

$$tdc^i_{corrected}(k) = tdc^i_{raw}(k) - LTC^i_j \tag{2.7}$$

2.5 Phase 1 and Phase 2

After running the experiment for 19 months, it was found that the concentration of the radon in the air inside the detector was high and was affecting the measurements. An anti-radon facility was introduced in September 2004. An airtight tent was constructed around the detector in order to prevent the radon diffusing through glue joints, and an air-cleaning system was installed to send radon-free air into the detector. The air-cleaner consisted of charcoal which traps the radon long enough to decay to a stable isotope (^{222}Rn has $T_{1/2} \approx 3.8$ days). As a result, the concentration level was reduced by a factor of ≈ 6 (Fig. 2.11). The pre- and post- anti-radon system installation periods were named as Phase 1 and Phase 2 respectively. The data acquisition time during these periods were

$$\text{Phase1} = 397.71 \text{ days} \tag{2.8}$$

$$\text{Phase2} = 1250.39 \text{ days} \tag{2.9}$$

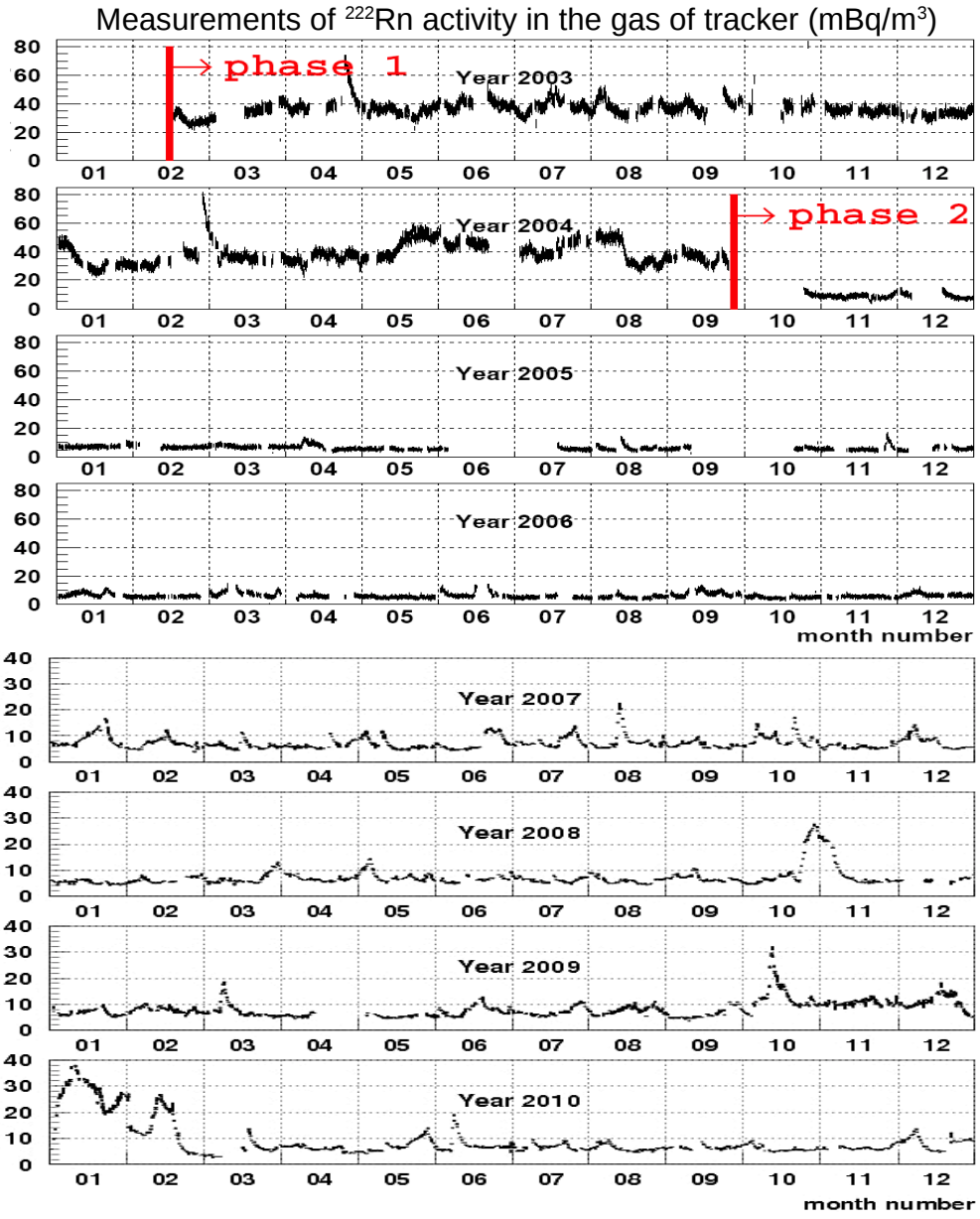

Figure 2.11: Total Rn activity inside the detector before and after the installation of the anti-radon facility [12].

Chapter 3

General Analysis Technique

3.1 Monte Carlo

A Monte Carlo (MC) comparison method is used to analyze the data. All the MC samples are generated by DECAY0 (which is a different version of DECAY4 [18]). After the kinematics of $\beta\beta$ and background events are simulated by DECAY0, NEMOS (which is based on GEANT-3.21 [19]) generates a full description of the detector and particle tracks including processes such as energy loss, scattering etc., according to their cross-sections. The simulated events have the same format as the data, hence they can be reconstructed identically.

3.2 Reconstruction of Data and Monte Carlo

The reconstruction of data and MC is done almost identically by NEMOR [20]. In both cases, a track is reconstructed if there are more than three hits on

Geiger layers and two of these are in adjacent layers. The track fitting program connects those layers to reconstruct a helical track of a charged particle. The best-fit track is then used to identify the particle by its curvature, length etc. (Sec. 3.3). During this process, the information of the experimental status of each data acquisition period, for example the status of the detector, energy and time calibration efficiencies and resolutions for individual calorimeter blocks, is applied only to MC via the NEMO database.

3.3 Particle Identification

The tracks of charged particles are bent due to the magnetic field (Sec 2.1) which is used to discriminate electrons and positrons. α particles are identified by their short traveling distance ($\approx$20 cm) before quenching in the gas. A photon can be identified by a scintillator hit without an associated track. A Time of Flight (TOF) calculation is also used to discriminate the internal events and the external events. (see Sec. 3.4.1)

3.3.1 Measurement of Photon Energy

Since photons are more likely to be scattered and deposit energy on more than one PMT, a sum of energies deposited in a "photon cluster" (Fig. 3.1) is used as the energy of a photon. In order to distinguish a photon's scintillator hit from noise, the scintillator hit must be isolated. The definition of the isolated hit is shown in Fig 3.2.

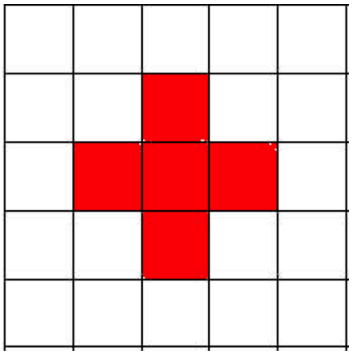

Figure 3.1: Sum of energies deposited on the highlighted PMTs by a photon is defined as an energy of a photon.

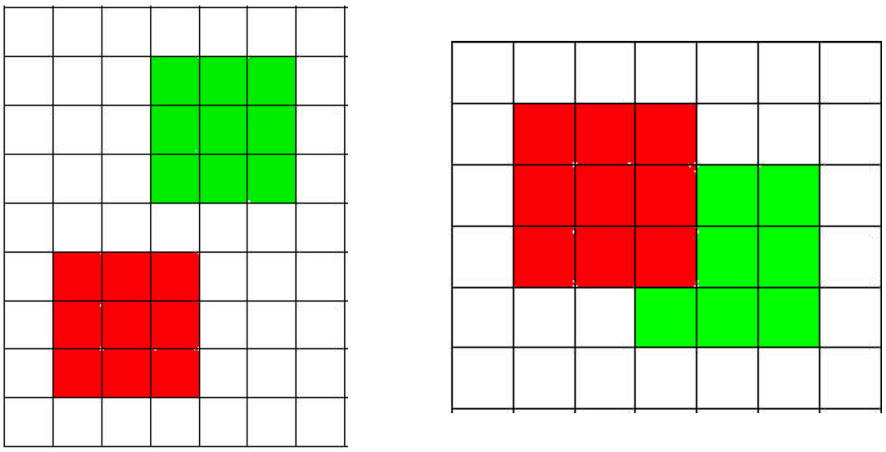

(a) (b)

Figure 3.2: Examples of (a) isolated photon clusters and (b) a non-isolated photon cluster.

3.4 Statistical Technique

A C++/ROOT [21] based statistical analysis program ROOTANA is specifically constructed for the NEMO-3 experiment and is used for most of the analysis in this dissertation. It is capable of performing statistical techniques such as TOF selection (Sec. 3.4.1) and likelihood fitting of MC to data (Sec. 3.4.2).

3.4.1 TOF probability

An event which has one electron crossing the foil can mimic an event which has two electrons coming from the foil. To discriminate those events, a TOF probability is calculated. For a pair of tracks with lengths l_1 and l_2 with associated energy deposits of E_1 and E_2 on the calorimeter, the internal and the external TOF differences are calculated theoretically by

$$\Delta t^{th}_{int} = \frac{l_1}{\beta_1} - \frac{l_2}{\beta_2}, \tag{3.1}$$

$$\Delta t^{th}_{ext} = \frac{l_1}{\beta_1} + \frac{l_2}{\beta_2}, \tag{3.2}$$

where β_i is the speed of the particle $i = 1, 2$ and defined as

$$\beta_i = \frac{\sqrt{E_i\left(E_i + 2m_e\right)}}{E_i + m_e} \tag{3.3}$$

assuming the particle mass is the electron mass m_e. For a photon accompanied with the emission of an electron, $\beta = 1$ and l is the distance between the center of the photon cluster and the vertex on the foil where the associated electron's track is found. The TOF $t^{TDC}_{int/ext}$ is experimentally measured by the TDC. From the theoretical and experimental TOF values, the following

variable is calculated for both the internal and external origin hypotheses,

$$\chi^2_{int/ext} = \frac{\left(\Delta t^{TDC}_{int/ext} - \Delta t^{th}_{int/ext}\right)^2}{\sigma^2_{TOF}}. \tag{3.4}$$

The uncertainty σ_{TOF} is expressed as

$$\left(\sigma_{TOF}\right)^2 = \sum_{i=1}^{2}\left[\left(\frac{l_i m_e^2}{\beta_i E_i(E_i+m_e)(E_i+2m_e)}\right)^2 \sigma_E^2 + \left(\frac{1}{\beta_i}\right)^2 \sigma_l^2 + \sigma^2_{t_i^{TDC}} + \sigma^2_{t_i^{LTC}}\right] \tag{3.5}$$

where σ_E, σ_l, $\sigma_{t_i^{TDC}}$ and $\sigma_{t_i^{LTC}}$ are uncertainties in energy measurements, track length calculation, time measured by TDC and LTC, respectively. The TOF probability $P_{int/ext}$ is given by

$$P_{int/ext}\left(\chi^2_{int/ext}\right) = 1 - \frac{2}{\sqrt{\pi}}\int_0^{\chi^2_{int/ext}} e^{x^2} dx, \tag{3.6}$$

where x is

$$x = \frac{1}{1+\sqrt{2\chi^2_{int/ext}}}. \tag{3.7}$$

3.4.2 Fitting Monte Carlo Events to Data

ROOTANA uses a maximum-likelihood estimation (MLE) [22] to fit the MC normalization to the data. MLE treats each bin of the energy distribution as an independent channel, therefore, it takes into account the shape of the distribution. In the i^{th} bin, MC predicts the number of events to be the sum of the signal (s_i) and backgrounds (b_i). Following Poisson statistics, the probability P_i of obtaining d_i events is given by

$$P_i = \frac{e^{-(s_i+b_i)}\left(s_i+b_i\right)^{d_i}}{d_i!}. \tag{3.8}$$

The likelihood (L) is defined as

$$L = \prod_{i=1}^{n} P_i, \tag{3.9}$$

where n is the number of bins in the histogram. The logarithm of the function is written as

$$\ln L = \sum_{i=0}^{n} \left[-\left(s_i + b_i\right) + d_i \ln\left(s_i + b_i\right) - \ln(d_i!) \right]. \tag{3.10}$$

The maximum can be found by setting the derivative with respect to the total number of signal events $\mathcal{S} = \sum_i s_i$ to be zero

$$\frac{\partial \ln L}{\partial \mathcal{S}} = -1 + \sum_{i=0}^{n} \left(\frac{d_i}{s_i + b_i} \frac{\partial s_i}{\partial \mathcal{S}} \right) = 0. \tag{3.11}$$

Eq. 3.11 is solved numerically to obtain S. Since L follows the χ^2 distribution, the standard deviation σ is determined by solving the following equation numerically;

$$\ln L(\mathcal{S}) - \ln L(\mathcal{S} \pm \Delta\mathcal{S}) = \frac{1}{2}. \tag{3.12}$$

Chapter 4

Construction of the Background Model

4.1 Background Events

The half-life $T^{0\nu}_{1/2}$ is expected to be $> 10^{26}$ years, whereas natural radioactivity has a typical $T_{1/2} < 10^{10}$ years. Therefore, it is important to understand the background processes that mimic the $\beta\beta$ signal. There are two types of non-$\beta\beta$ events that produce two-electron events originating in the foil. One is the internal background, which has its origin inside the source foil, and the other is the external background, which has its origin located outside the foil. The internal backgrounds are mostly due to the presence of radioactive isotopes in the foil. As shown in Fig. 4.1a, they can undergo one of the following processes to mimic $\beta\beta$ events [23]:

- A β decay to an excited state. Then the daughter nucleus de-excites and emits an electron by an internal conversion.

- A β decay where the β particle undergoes Møller scattering off another electron in the foil.
- A β-γ cascade where the photon produces an extra electron via Compton scattering.

The external backgrounds are mostly produced by a photon coming from outside the foil. As shown in Fig. 4.1b, they undergo interactions includes such as:

- Pair production to create an electron and a positron which can be misidentified as an electron.
- Double Compton scatterings.
- Compton scattering and the scattered electron undergoes Møller scattering.
- Photoelectric Effect and the photoelectron undergoes Møller scattering.
- Compton scattering and the scattered photon causes a photoelectric effect.

Some of the external background components originating from radon and thoron in the air inside the detector can undergo processes similar to the internal backgrounds. During the experiment, the type of the external backgrounds are given names, such as exbg2, and are explained in Sec. 4.3.

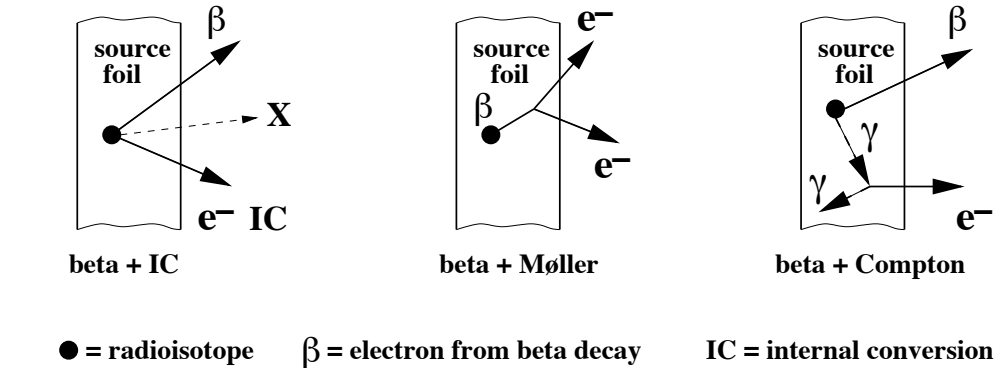

(a)

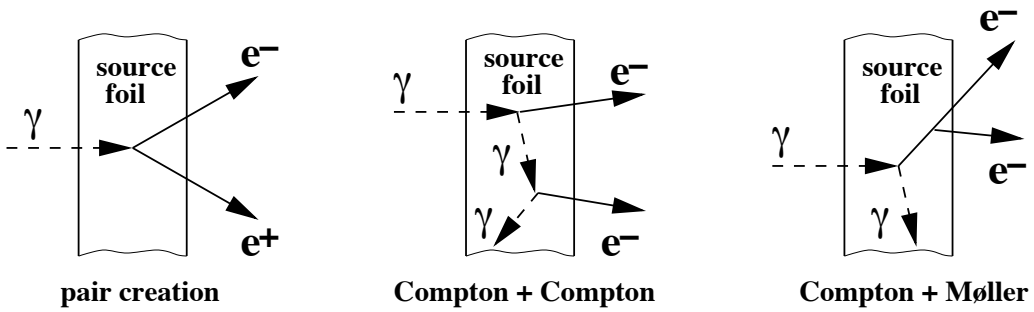

(b)

Figure 4.1: Diagram illustrating (a) internal background production and (b) external background production. Photoelectric effect can be considered as a Compton scattering with no scattered photon [23].

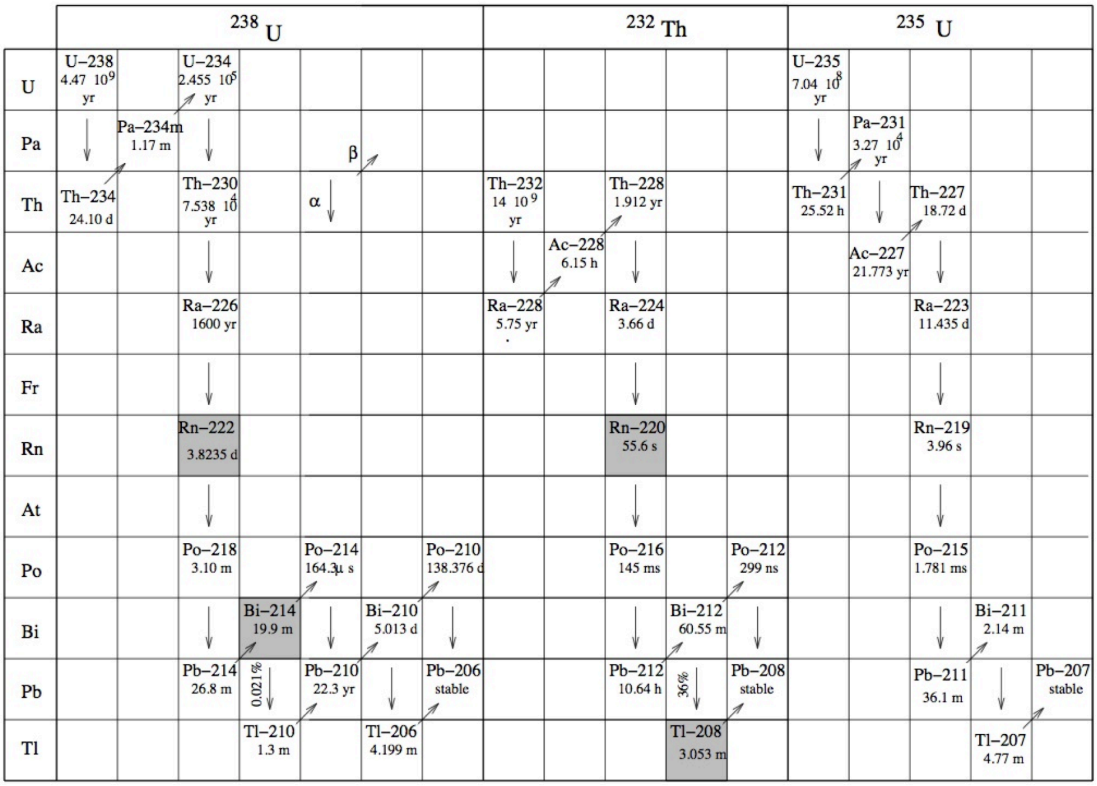

Figure 4.2: The decay series of ^{238}U, ^{232}Th and ^{235}U. They are the main sources of natural radioactivity [4].

4.2 Internal Background of the ^{150}Nd Foil

Radioactive isotopes can mimic $\beta\beta$ events as described in Sec. 4.1. Their activities are estimated by investigating different final states (one electron plus one photon, one electron plus two photons and one electron events).

4.2.1 The Hot Spots

The "hot spots", which are the spots on the ^{150}Nd foil where contamination of background isotopes are especially high, were identified by previous studies [15, 24]. The coordinates of them are defined as:

(a) $1.820 < \phi < 1.827$ rad, $34 < \mathrm{z} < 42$ cm

(b) $1.836 < \phi < 1.842$ rad, $6 < \mathrm{z} < 12$ cm

(c) $1.801 < \phi < 1.802$ rad, $52.8 < \mathrm{z} < 55$ cm

(d) $1.815 < \phi < 1.827$ rad, $104 < \mathrm{z} < 110$ cm

The hot spots (a), (b) and (c) are determined by using the one electron plus one photon channel (Fig. 4.3) and (d) is determined by the one electron channel as shown in Fig. 4.4.

4.2.2 Measurement of BiPo Activity

^{214}Bi and ^{214}Po are in the decay chain of ^{238}U as shown in Fig. 4.2. The majority (99.98 %) of ^{214}Bi decays to ^{214}Po via α decay, and immediately afterwards the daughter nucleus emits a β particle ($T_{1/2} \approx 164\,\mu$s). This event cascade is named as BiPo and its activity for the ^{150}Nd foil was measured to be

$$\mathrm{A(BiPo)} = 0.187 \pm 0.05\,\mathrm{mBq} \tag{4.1}$$

by studying one electron plus one α events [23]. The hot spots are not removed for this measurement.

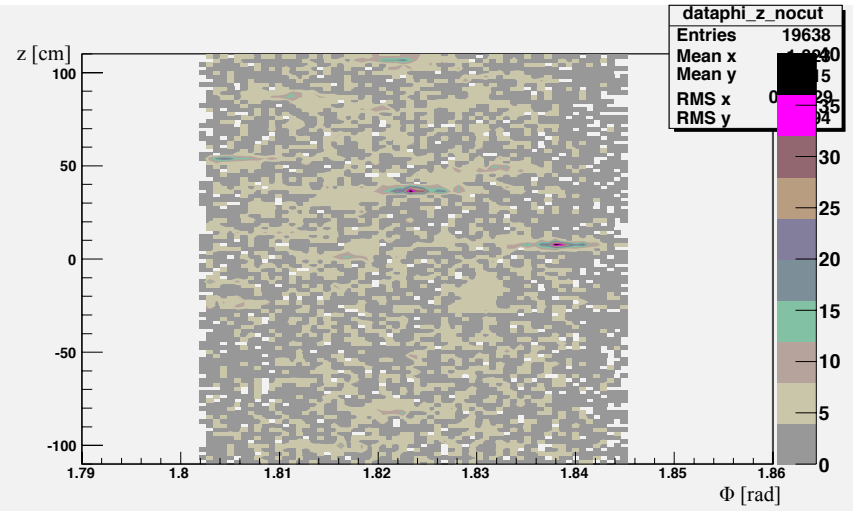

(a)

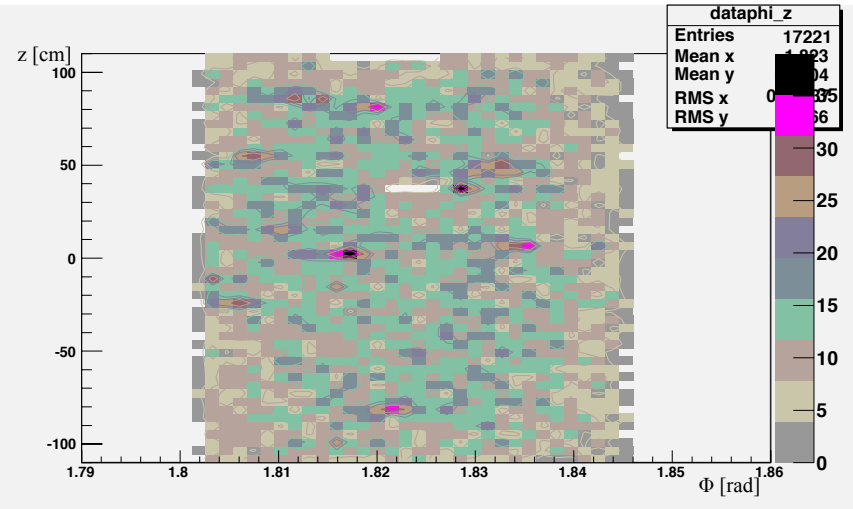

(b)

Figure 4.3: Distribution of event vertices on the foil for one electron plus one photon channel (a) with the hot spots and (b) without the hot spots.

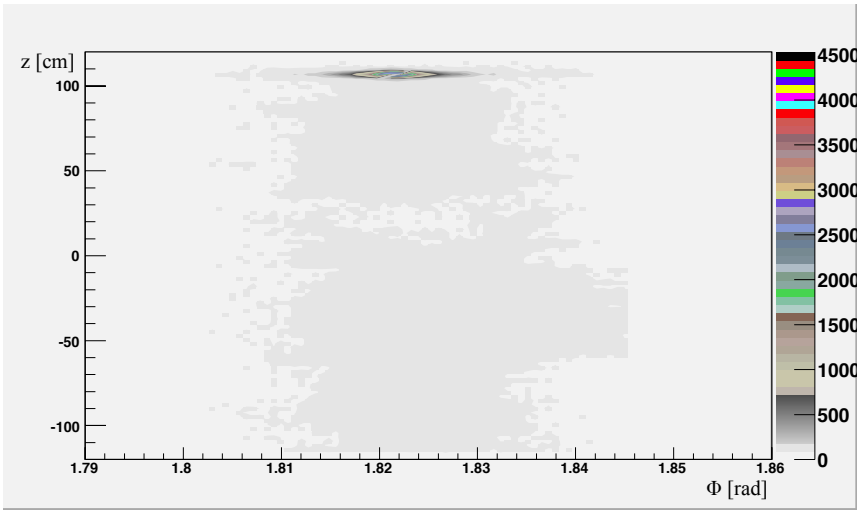

(a)

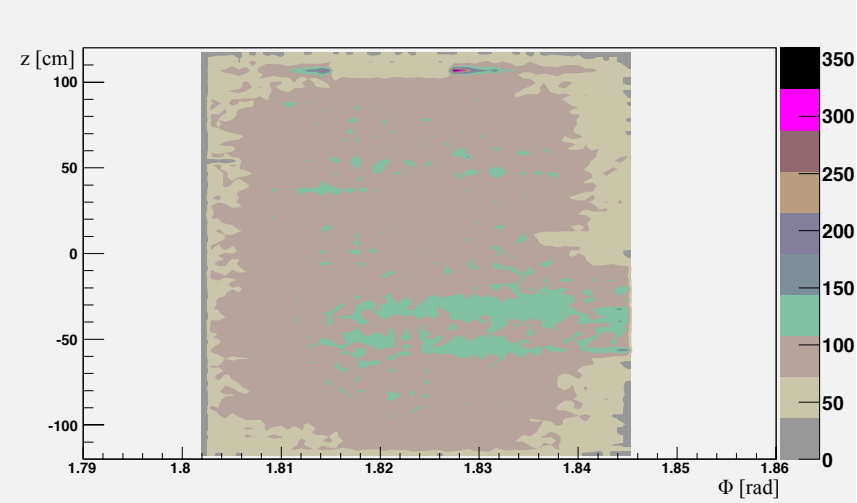

(b)

Figure 4.4: Distribution of event vertices on the foil for one electron channel (a) with the hot spots and (b) without the hot spots.

4.2.3 One Electron - One Photon Channel

The contaminations of the following isotopes are measured with these decay channels:

- ^{208}Tl: it principally decays via emission of one electron and two photons (Sec. 4.2.4). However, one of the photons may be lost due to the finite acceptance of the detector.
- ^{207}Bi: it decays to the excited states of ^{207}Pb via electron capture. Then, the ^{207}Pb emits a photon to be in its ground state.
- ^{152}Eu: it can decay to several exited states of either ^{152}Gd or ^{152}Sm through a β^--decay (27%) or an electron capture (73%), respectively. The daughter nuclei then de-excite by the emission of a photon.
- ^{154}Eu: it undergoes a β^--decay and the daughter nucleus ^{154}Gd produces a photon in a similar way to ^{152}Eu.

The following criteria are applied to select one electron plus one photon events:

- Only one track of a negatively charged particle with an associated scintillator hit in the energy range $0.2 < E_e < 4.0$ MeV is found.
- Run status and PMT status are both good.
- The track originates inside the ^{150}Nd foil geometry as described in Sec. 2.2.1, but not from the hot spots, which are defined in Sec. 4.2.1.
- The charged particle hits at least one of the first two layers of the Geiger cells.

- One photon cluster with energy $E_\gamma > 0.2$ MeV is detected.
- The energy sum of all other photon clusters is < 0.2 MeV.
- The length of the electron trajectory is > 50 cm.
- The internal TOF probability is > 4 % and the external TOF probability is < 1 %.

Activity of ^{208}Tl

^{208}Tl occurs naturally in the ^{232}Th chain. The activity is driven by the large half-life of ^{232}Th, hence ^{208}Tl has a constant activity. Since ^{228}Ac and ^{212}Bi are in the same decay chain and 36% of ^{212}Bi decays to ^{208}Tl, the activities of ^{228}Ac and ^{212}Bi are estimated from the activity of ^{208}Tl. In addition to the selection criteria described above, the events are required to have a photon which has energy > 2.0 MeV for the ^{208}Tl measurement. In this energy region, only ^{208}Tl and ^{214}Bi on the surface of the wires dominate and all the isotopes with unknown activities do not contribute. From the distribution shown in Fig. 4.5 (the details of activity measurements shown in this and subsequent figures are given in Appendix A), the activity of ^{208}Tl is measured to be

$$\mathrm{A}(^{208}\mathrm{Tl}) = 0.61 \pm 0.07 \text{ (stat) mBq.} \tag{4.2}$$

for Phase 1 and

$$\mathrm{A}(^{208}\mathrm{Tl}) = 0.61 \pm 0.04 \text{ (stat) mBq.} \tag{4.3}$$

for Phase 2. Therefore,

$$\mathrm{A}(^{212}\mathrm{Bi},^{228}\mathrm{Ac}) = 1.69 \pm 0.20 \text{ (stat) mBq} \tag{4.4}$$

$$\mathrm{A}(^{212}\mathrm{Bi},^{228}\mathrm{Ac}) = 1.69 \pm 0.11 \text{ (stat) mBq} \tag{4.5}$$

for Phase 1 and Phase 2, respectively

Activity of ^{207}Bi

In order to measure the activity of ^{207}Bi, which emits a photon of known energy, the following selection criteria are added:

- $0.70 < E_e < 1.10$ MeV
- $0.25 < E_\gamma < 0.60$ MeV

In this region, ^{207}Bi dominates over the other backgrounds. The activity of ^{207}Bi is estimated to be

$$\mathrm{A}(^{207}\mathrm{Bi}) = 11.7 \pm 0.5 \text{ (stat) mBq (Phase1)} \tag{4.6}$$

$$\mathrm{A}(^{207}\mathrm{Bi}) = 11.0 \pm 0.2 \text{ (stat) mBq (Phase2)} \tag{4.7}$$

as shown in Fig. 4.6.

Activities of ^{152}Eu and ^{154}Eu

Both ^{152}Eu and ^{154}Eu are fitted simultaneously to the energy spectrum of the photon shown in Fig. 4.7. ^{152}Eu and ^{154}Eu are fitted by the maximum-likelihood method (Sec. 3.4.2). The activities of ^{152}Eu and ^{154}Eu are measured to be

$$\mathrm{A}(^{152}\mathrm{Eu}) = 2.06 \pm 0.15 \text{ (stat) mBq.} \tag{4.8}$$

$$\mathrm{A}(^{154}\mathrm{Eu}) = 0.16 \pm 0.02 \text{ (stat) mBq.} \tag{4.9}$$

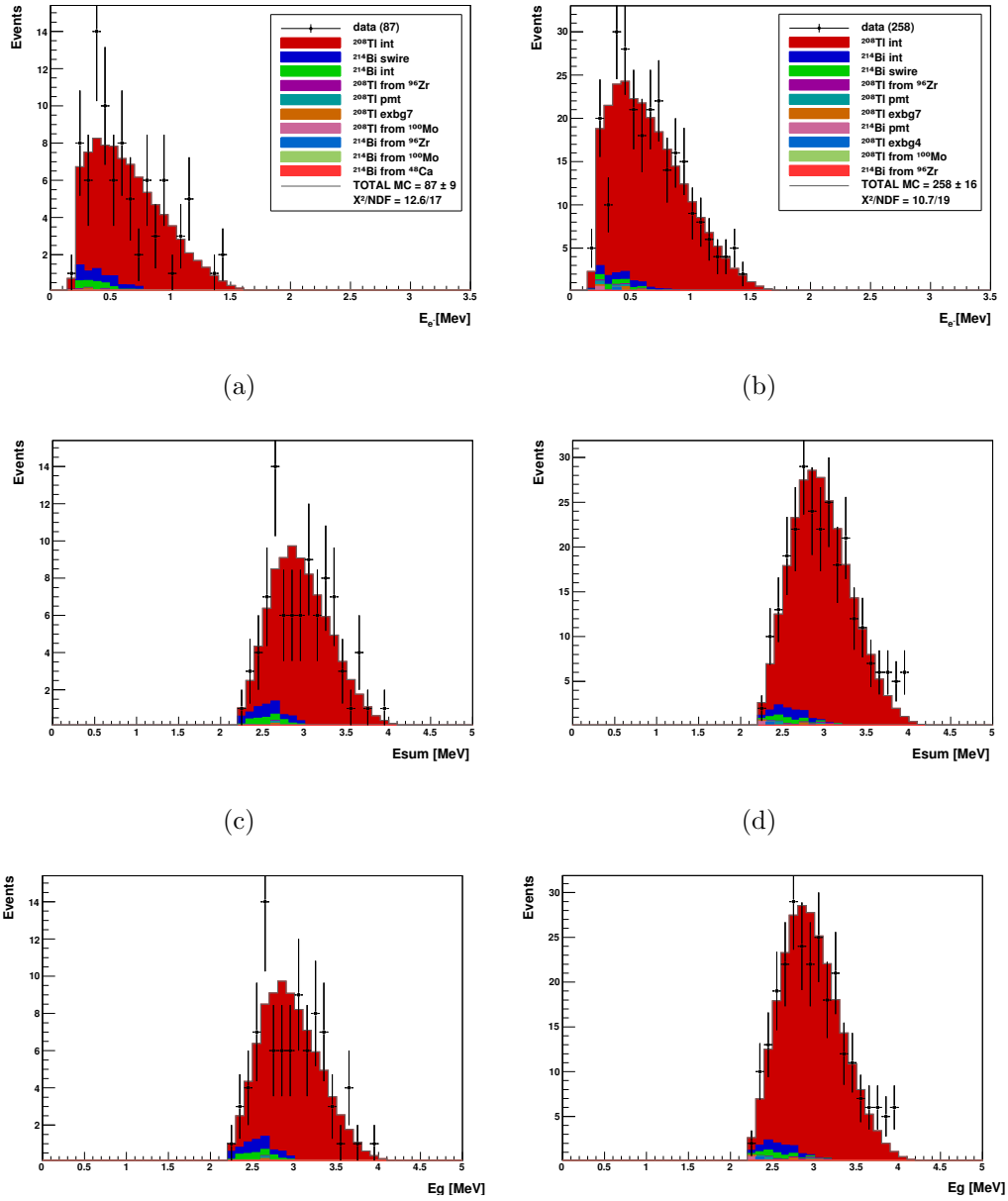

Figure 4.5: (a, b) electron energy spectrum; (c, d) photon energy spectrum; (e, f) energy sum of events with $E_\gamma > 2.0$ MeV. (a, c, e) Phase 1 data and they are described by the legend in (a); (b, d, f) Phase 2 data and they are described by the legend in (b).

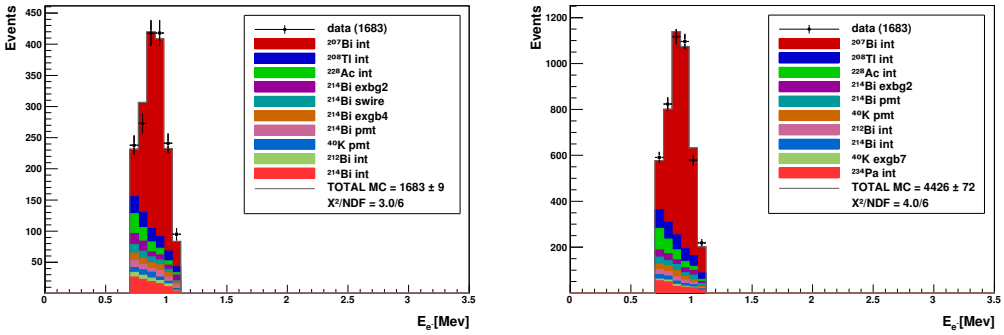

(a) (b)

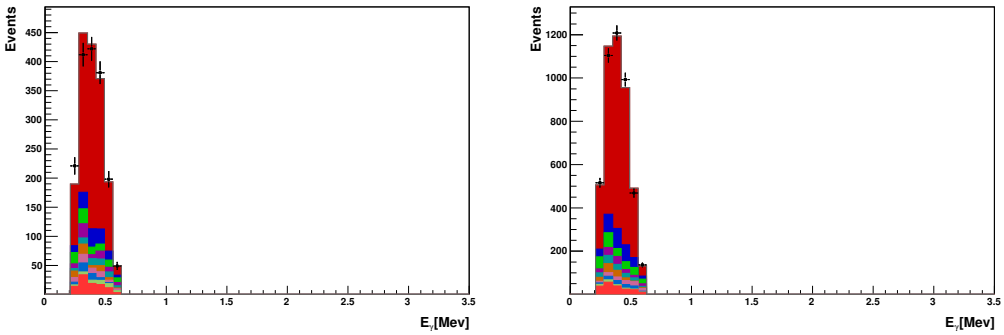

(c) (d)

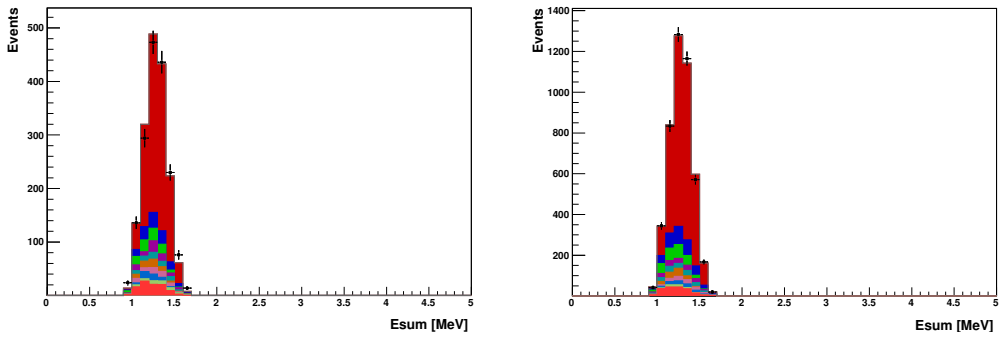

(e) (f)

Figure 4.6: (a, b) electron energy spectrum; (c, d) photon energy spectrum; (e, f) energy sum of the selected region $0.7 < E_e < 1.10$ MeV and $0.25 < E_\gamma < 0.60$ MeV. (a, c, e) Phase 1 data and they are described by the legend in (a); (b, d, f) Phase 2 data and they are described by the legend in (b).

for phase 1 and

$$\mathrm{A}(^{152}\mathrm{Eu}) = 1.88 \pm 0.09 \text{ (stat) mBq.} \tag{4.10}$$

$$\mathrm{A}(^{154}\mathrm{Eu}) = 0.93 \pm 0.05 \text{ (stat) mBq.} \tag{4.11}$$

for Phase 2.

4.2.4 One Electron - Two Photon Channel

^{208}Tl decays to an excited state of ^{207}Pb with an emission of a β particle. The daughter nucleus emits two photons to de-excite to its ground state. A schematic diagram for this decay is shown in Fig 4.8. The initial photon has the energy of either 0.58 MeV or 0.86 MeV and the second photon has an energy of 2.6 MeV. Similarly, 17.6 % of ^{214}Bi decay to ^{214}Po, which produces photons with an energy of 0.61 MeV and 1.12 MeV. To enhance the signal of ^{208}Tl, the following event selections are applied:

- Only one track of a negatively charged particle with an associated scintillator hit of the energy > 0.2 MeV is found.
- Run status and PMT status are both good.
- The track originates inside the ^{150}Nd foil geometry as described in Sec. 2.2.1, but not from the hot spots, which are defined in Sec. 4.2.1.
- The charged particle hits at least one of the first two layers of the Geiger cells.
- Two photons are detected. The one with lower energy is required to have $E_{\gamma_1} > 0.35$ MeV and the one with higher energy is required to have $E_{\gamma_2} > 1.8$ MeV.

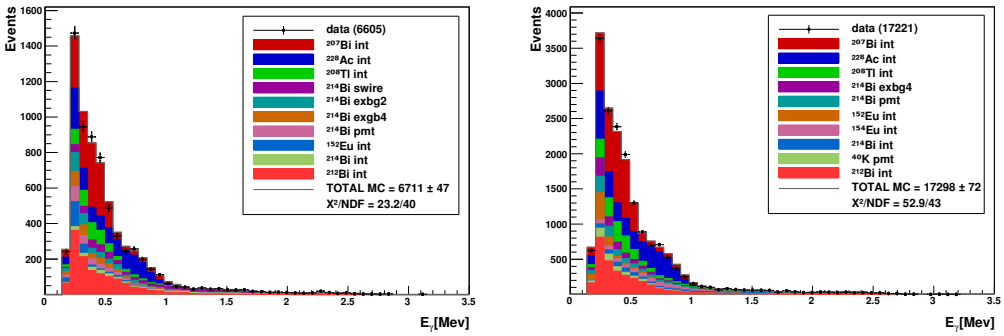

(a)

(b)

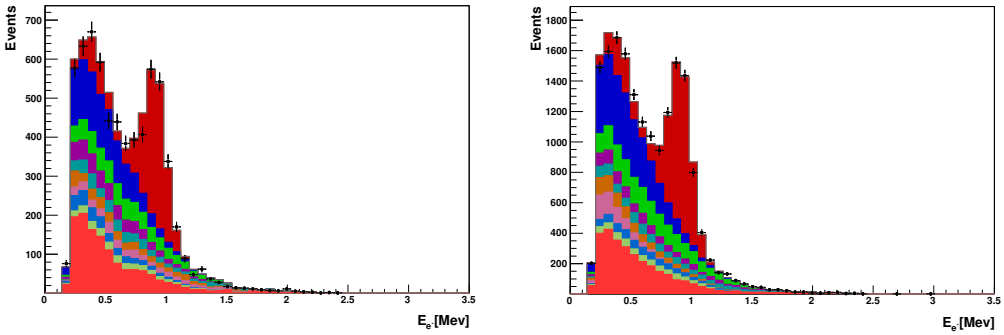

(c)

(d)

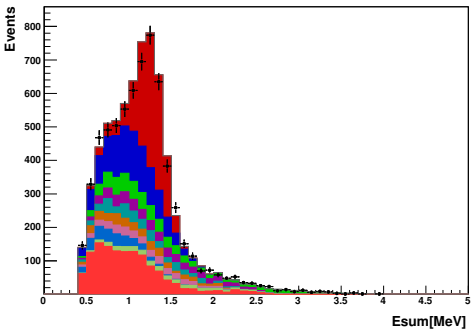

(e)

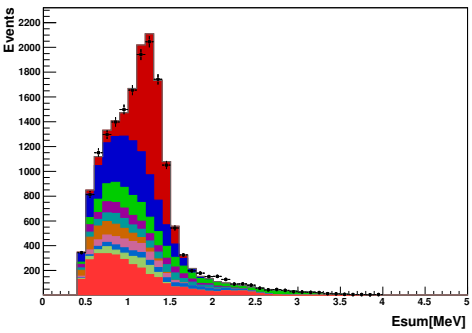

(f)

Figure 4.7: (a, b) photon energy spectrum; (c, d) electron energy spectrum; (e, f) energy sum spectrum for whole region. (a, c, e) Phase 1 data and they are described by the legend in (a); (b, d, f) Phase 2 data and they are described by the legend in (b).

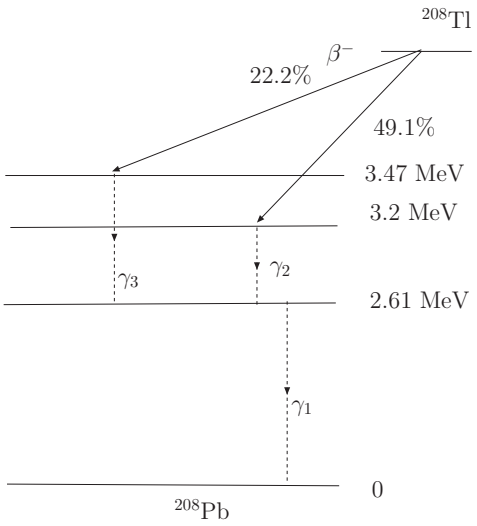

Figure 4.8: Decay scheme of ^{208}Tl [15].

- The energy sum of all other photon clusters is < 0.2 MeV.
- The length of the particle trajectory is > 50 cm.
- The internal TOF probability is > 4 % and the external TOF probability is < 1 %.

From the distribution shown in Fig. 4.9, the activity of ^{208}Tl was measured to be

$$\mathrm{A}(^{208}\mathrm{Tl}) = 0.50 \pm 0.09 \text{ (stat) mBq} \tag{4.12}$$

$$\mathrm{A}(^{208}\mathrm{Tl}) = 0.66 \pm 0.06 \text{ (stat) mBq} \tag{4.13}$$

for Phase 1 and 2, respectively. Hence,

$$\mathrm{A}(^{212}\mathrm{Bi},^{228}\mathrm{Ac}) = 1.39 \pm 0.25 \text{ (stat) mBq} \tag{4.14}$$

for Phase 1 and

$$\mathrm{A}(^{212}\mathrm{Bi},^{228}\mathrm{Ac}) = 1.83 \pm 0.17 \text{ (stat) mBq} \tag{4.15}$$

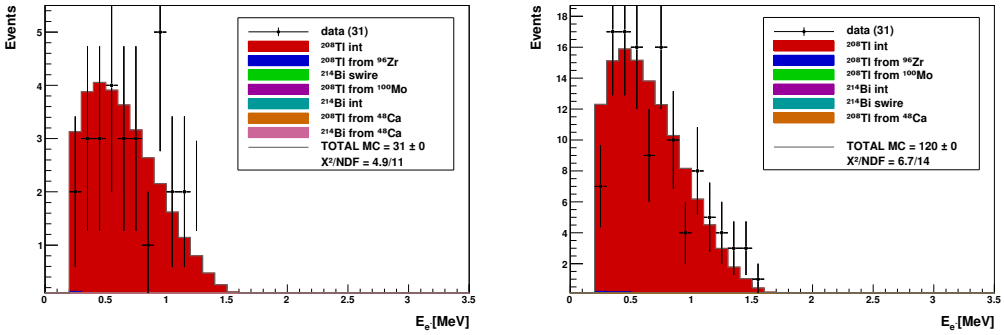

(a)

(b)

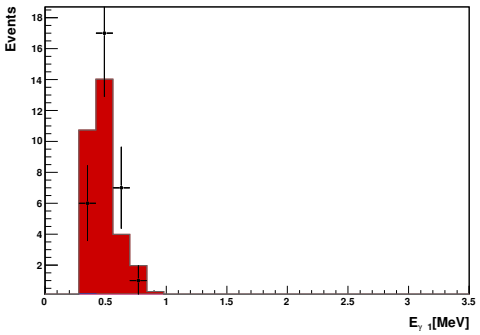

(c)

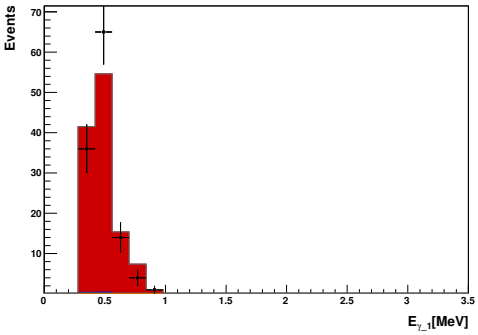

(d)

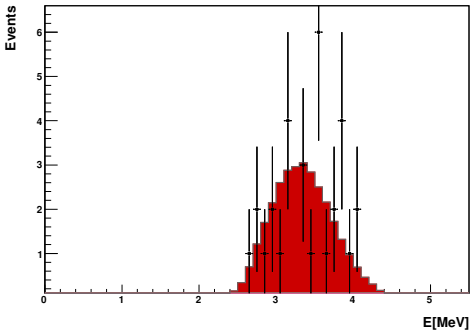

(e)

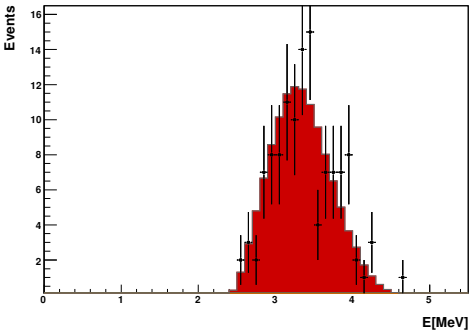

(f)

Figure 4.9: (a, b) electron energy spectrum; (c, d) γ_1 energy spectrum; (e, f) energy sum of events with $E_{\gamma_1} > 0.35$ MeV and $E_{\gamma_2} > 1.8$ MeV. (a, c, e) Phase 1 data and they are described by the legend in (a); (b, d, f) Phase 2 data and they are described by the legend in (b).

for Phase 2 were determined.

4.2.5 Estimation of Systematic Uncertainties

The activity of ^{208}Tl is measured both in the one electron one photon channel (Sec. 4.2.3) and one electron two photon channel (Sec. 4.2.4). By calculating the average and the deviation from the average as systematic uncertainty, the activity of ^{208}Tl is measured to be

$$\mathrm{A}(^{208}\mathrm{Tl}) = 0.55 \pm 0.06 \text{ (sys) mBq.} \tag{4.16}$$

$$\mathrm{A}(^{208}\mathrm{Tl}) = 0.63 \pm 0.03 \text{ (sys) mBq.} \tag{4.17}$$

for Phase 1 and 2, respectively. This implies that

$$\mathrm{A}(^{212}\mathrm{Bi},^{228}\mathrm{Ac}) = 1.54 \pm 0.15 \text{ (sys) mBq} \tag{4.18}$$

for Phase 1 and

$$\mathrm{A}(^{212}\mathrm{Bi},^{228}\mathrm{Ac}) = 1.76 \pm 0.06 \text{ (sys) mBq} \tag{4.19}$$

for Phase 2. By using the activities for ^{208}Tl, ^{212}Bi and ^{228}Ac obtained from the one electron two photon channel (Sec. 4.2.4) and refitting to the one electron one photon distributions, the activities of ^{207}Bi, ^{152}Eu and ^{154}Eu are reevaluated. By calculating the deviation between them and the original values, the activities of ^{207}Bi, ^{152}Eu and ^{154}Eu are found to be

$$\mathrm{A}(^{207}\mathrm{Bi}) = 11.9 \pm 0.5 \text{ (stat)} \pm 0.2 \text{ (sys) mBq} \tag{4.20}$$

$$\mathrm{A}(^{152}\mathrm{Eu}) = 2.40 \pm 0.15 \text{ (stat)} \pm 0.34 \text{ (sys) mBq} \tag{4.21}$$

$$\mathrm{A}(^{154}\mathrm{Eu}) = 0.23 \pm 0.02 \text{ (stat)} \pm 0.07 \text{ (sys) mBq} \tag{4.22}$$

for Phase 1 and

$$\mathrm{A}(^{207}\mathrm{Bi}) = 10.9 \pm 0.2\ (\mathrm{stat}) \pm 0.1\ (\mathrm{sys})\ \mathrm{mBq} \tag{4.23}$$

$$\mathrm{A}(^{152}\mathrm{Eu}) = 1.68 \pm 0.09\ (\mathrm{stat}) \pm 0.20\ (\mathrm{sys})\ \mathrm{mBq} \tag{4.24}$$

$$\mathrm{A}(^{154}\mathrm{Eu}) = 0.81 \pm 0.06\ (\mathrm{stat}) \pm 0.12\ (\mathrm{sys})\ \mathrm{mBq} \tag{4.25}$$

for Phase 2.

4.2.6 One Electron Channel

Internal ^{234m}Pa, internal ^{40}K and ^{210}Bi on the surface of the wires undergoes single β decay to the ground states of the daughter nuclei. Hence, the activities are measured in the one electron channel. The following selection criteria are applied:

- Only one track of a negatively charged particle is found. The track must have an associated scintillator hit with the energy > 0.5 MeV. If the LEC is applied, the corrected energy is required to be > 0.5 MeV.
- Run status and PMT status are both good.
- The track originates inside the ^{150}Nd foil geometry as described in Sec. 2.2.1, but not from the hot spots, which are defined in Sec. 4.2.1.
- The length of the particle trajectory is > 50 cm.
- The charged particle hit at least one of the first two layers of the Geiger cells.

The three activities are measured by fitting simultaneously to the electron energy spectrum with the maximum likelihood method. For Phase 1, the

activities

$$\mathrm{A}(^{40}\mathrm{K}) = 10.3 \pm 0.1\ (\mathrm{stat}) \pm 0.8\ (\mathrm{sys})\ \mathrm{mBq} \tag{4.26}$$

$$\mathrm{A}(^{234\mathrm{m}}\mathrm{Pa}) = 2.07 \pm 0.03\ (\mathrm{stat}) \pm 0.13\ (\mathrm{sys})\ \mathrm{mBq} \tag{4.27}$$

$$\mathrm{A}(^{210}\mathrm{Bi}) = 1.87 \pm 0.04\ (\mathrm{stat}) \pm 0.29\ (\mathrm{sys})\ \mathrm{Bq} \tag{4.28}$$

are found from Fig. 4.10. Similarly for Phase 2,

$$\mathrm{A}(^{40}\mathrm{K}) = 10.2 \pm 0.1\ (\mathrm{stat}) \pm 0.2\ (\mathrm{sys})\ \mathrm{mBq} \tag{4.29}$$

$$\mathrm{A}(^{234\mathrm{m}}\mathrm{Pa}) = 1.85 \pm 0.02\ (\mathrm{stat}) \pm 0.03\ (\mathrm{sys})\ \mathrm{mBq} \tag{4.30}$$

$$\mathrm{A}(^{210}\mathrm{Bi}) = 1.59 \pm 0.02\ (\mathrm{stat}) \pm 0.05\ (\mathrm{sys})\ \mathrm{Bq} \tag{4.31}$$

are determined. The systematic uncertainties are found by comparing the results which the LEC is applied.

4.2.7 Summary

The activities of internal backgrounds measured above are shown in Tab. 4.1.

4.3 External Background of the ^{150}Nd Foil

Tab. 4.2 shows a list of the sources of external backgrounds and corresponding activities [23]. In order to validate this model, one electron plus one photon events are investigated with the following event selections:

- Only one track of a negatively charged particle with an associated scintillator hit in the energy range $0.2 < E_e < 4.0$ MeV is found.

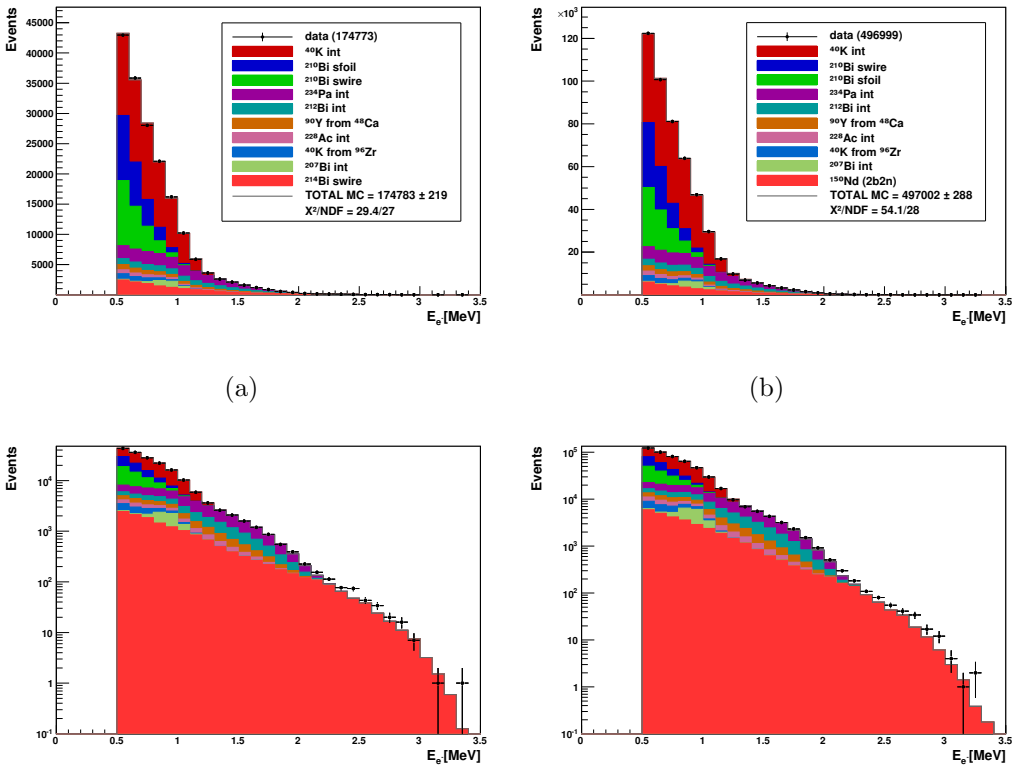

Figure 4.10: (a, b) electron energy spectrum; (c, d) on logarithmic scale. (a, c) Phase 1 data and they are described by the legend in (a); (b, d) Phase 2 data and they are described by the legend in (b).

Isotope	Activity (mBq)		Method
	Phase 1	Phase 2	
^{214}Bi	0.187 ± 0.05		BiPo
^{214}Pb	0.187 ± 0.05		BiPo
^{208}Tl	0.55 ± 0.07 ± 0.06	0.63 ± 0.05 ± 0.03	eγ & eγγ
^{228}Ac	1.54 ± 0.23 ± 0.15	1.76 ± 0.14 ± 0.07	eγ & eγγ
^{212}Bi	1.54 ± 0.23 ± 0.16	1.76 ± 0.14 ± 0.07	eγ & eγγ
^{207}Bi	11.9 ± 0.5 ± 0.2	10.9 ± 0.2 ± 0.1	eγ
^{152}Eu	2.40 ± 0.15 ± 0.34	1.68 ± 0.09 ± 0.20	eγ
^{154}Eu	0.23 ± 0.02 ± 0.07	0.81 ± 0.05 ± 0.12	eγ
^{40}K	10.3 ± 0.1 ± 0.8	10.2 ± 0.1 ± 0.2	e
^{234m}Pa	2.07 ± 0.03 ± 0.13	1.85 ± 0.02 ± 0.03	e
^{210}Bi	1.87 ± 0.04 ± 0.29 Bq	1.59 ± 0.02 ± 0.05 Bq	e

Table 4.1: The activities of internal radioactive isotopes. The first uncertainty is statistical and the second systematic.

- Run status and PMT status are both good.
- The track originates inside the ^{150}Nd foil geometry as described in Sec. 2.2.1, but not from the hot spots, which are defined in Sec. 4.2.1.
- The charged particle hit at least one of the first two layers of the Geiger cells.
- One photon with energy $E_\gamma > 0.2$ MeV was detected.
- The energy sum of all other photon clusters is < 0.2 MeV.
- The length of the particle trajectory is > 50 cm.
- The external TOF probability is > 4 % and the internal TOF probability is < 1 %.

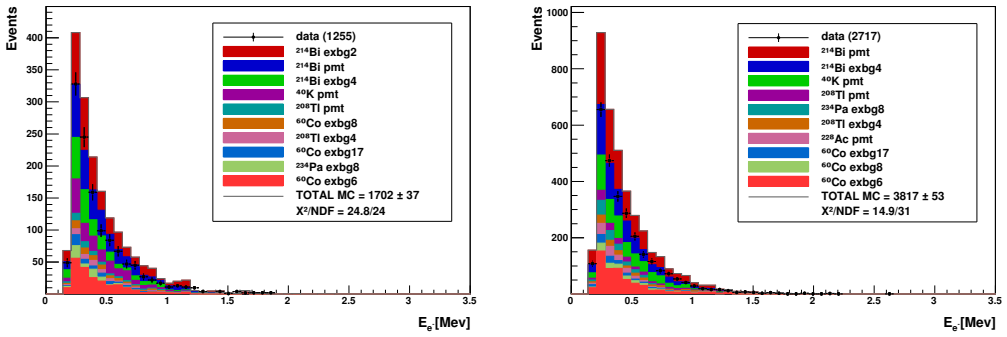

(a)

(b)

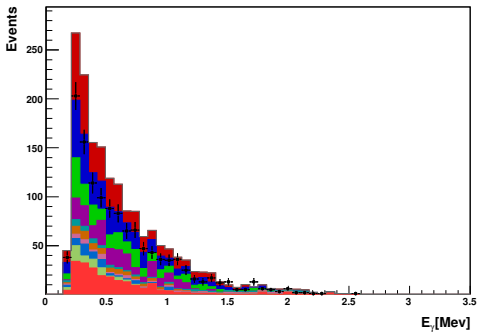

(c)

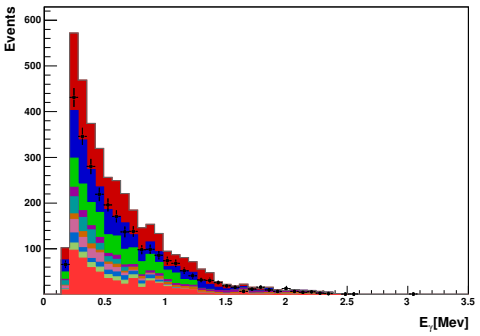

(d)

Figure 4.11: (a, b) electron energy spectrum; (c, d) photon energy spectrum of external one electron plus one photon events. (a, c) Phase 1 data; (b, d) Phase 2 data.

The internal backgrounds are normalized to the activities that are determined in the previous sections and the external backgrounds are normalized as described in Tab. 4.2. As shown in Fig. 4.11, the model describes the external events well.

Source	Isotope	Activity (Bq)	
		Phase 1	Phase 2
Air Under Iron Shield (exbg2)	^{214}Bi	566	0
	^{214}Pb	566	0
	^{208}Tl	11.5	0
Iron Shield (exbg4)	^{214}Bi	7.36×10^3	
	^{208}Tl	4.84×10^2	
	^{228}Ac	1.35×10^3	
Internal Tower (exbg6)	^{60}Co	29.4	18.4
Iron Petals (exbg7)	^{40}K	100	
	^{214}Bi	9.12	
	^{208}Tl	3.07	
	^{228}Ac	8.54	
	^{60}Co	6.09	
	^{234m}Pa	1.51×10^3	
PMT Shield (exbg8)	^{60}Co	23.3	14.6
	^{234m}Pa	3.42×10^3	
PMT Glass (exbg11)	^{40}K	1.08×10^3	
	^{214}Bi	324	
	^{208}Tl	27.0	
	^{228}Ac	72.7	
Copper Above Petals (exbg17)	^{60}Co	76.1	47.6
Inside Scintillator (sci)	^{40}K	7.17	
Scintillator Surface (ss)	^{210}Bi	30.4	
	^{214}Bi	0.38	
	^{214}Pb	0.38	
Wire Surface (sw)	^{210}Bi	9.93	8.92
	^{214}Bi	1.201	0.198
	^{214}Pb	1.201	0.198

Table 4.2: The list of external backgrounds [23]. Inside the brackets, the short hand notation for the type of the background used during the experiment is shown.

Chapter 5

Two Neutrino Double Beta Decay of ^{150}Nd

5.1 Definition of Half-life

The expected number of events, $N(t)$, can be calculated by;

$$N(t) = \varepsilon N_0 \left(1 - \exp\left[-\ln 2 \left(\frac{t}{T_{1/2}}\right)\right]\right), \tag{5.1}$$

where ε is the event selection efficiency, N_0 is the number of ^{150}Nd atoms in the foil and is equal to 1.462×10^{23}, t is the data collection time and $T_{1/2}$ is the half-life of a particular decay mode. Since $T_{1/2}$ is large, it can be approximated by

$$T_{1/2} = \varepsilon N_0 \ln 2 \left(\frac{t}{N(t)}\right). \tag{5.2}$$

5.2 Two Electron Channel

The following selection criteria are applied to maximize the signal to background ratio;

- Two isolated tracks of negatively charged particles are found. The tracks must have the associated scintillator hits with the energy > 0.2 MeV. If the LEC value is applied, the corrected energy was required to be > 0.2 MeV (Sec. 5.2.1).
- Run status and PMT status were both good.
- Particles hit the face and not the side of the scintillator.
- Tracks must originate inside the ^{150}Nd foil, but not from the hot spots. The definition of ^{150}Nd foil geometry is discussed in Sec. 5.2.1.
- Two tracks must have a common vertex with < 2 cm in the x-y plane and < 4 cm in the z direction.
- The internal TOF probability is $> 4\%$ and the external TOF probability is $< 1\%$.
- Tracks must have the length > 30 cm.
- The particles must pass through one of the first two Geiger layers.

5.2.1 Optimization of Selection Criteria

Optimization of the Foil Geometry

The resolution of the tracking detector is limited, thus a small portion of the ^{150}Nd events can be misidentified as events from the adjacent foils and vice

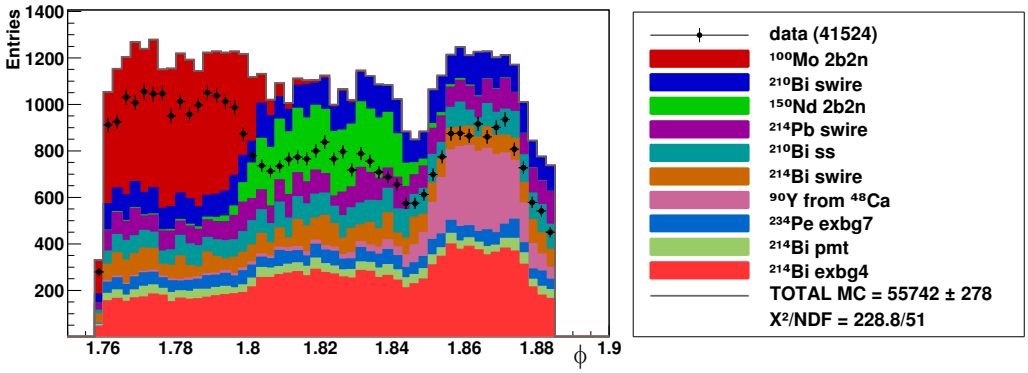

Figure 5.1: The distribution of MC events as a function of ϕ. As this does not include any cuts, MC does not describe the data well.

versa. Hence, the definition of the foil geometry is optimized to improve the product of the selection efficiency ε and the purity p. ε is taken from MC events and p is defined as

$$p = \frac{S}{S+B}, \tag{5.3}$$

where S is the number of signal MC events and B is the total number of background MC events. The ^{150}Nd foil is defined that $1.802 < \phi < 1.845$. The ϕ distribution of MC events is shown in Fig. 5.1. The boundary at $\phi = 1.802$ is adjacent to the ^{100}Mo foil and named as the "Left Boundary" The other side of the foil is adjacent to the foil consisting of ^{96}Zr and ^{48}Ca and named as the "Right Boundary".

Fig. 5.2 (a) shows that the real boundary is the optimal boundary for the analysis. However, (b) shows that it is better to shift ϕ from 1.845 to 1.847.

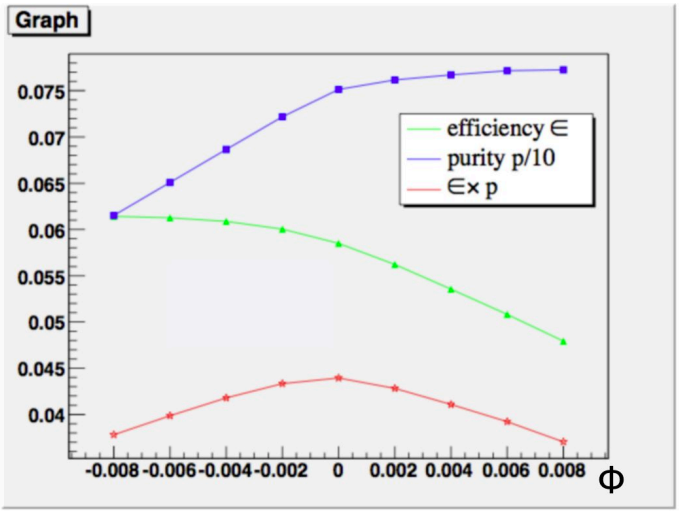

(a) "Left Boundary"

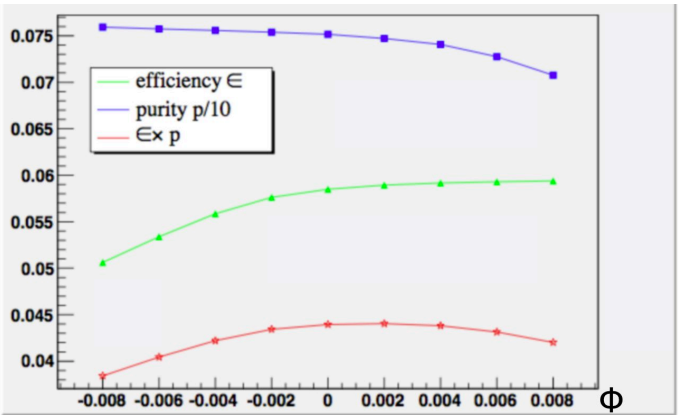

(b) "Right Boundary"

Figure 5.2: ε, p and the product $\varepsilon \times p$ for (a) "Left Boundary" and (b) "Right Boundary". p is scaled down by a factor of 10.

Optimization of Laser Energy Correction

In order to determine how the LEC (Sec. 2.4.3) should be used, the following methods are tested:

- Do not apply LEC value. - "No LEC"
- Apply LEC. If LEC is not available, use the uncorrected measurement of energy instead. - "LEC 140"
- Apply LEC. If LEC is not available, exclude the events from the final results. - "LEC 00"

As shown in Fig. 5.3, most of the correction values are $\leq |2\%|$ and Gaussian distributed with the peak at 1 i.e. no correction. LEC values are only applied to the data because MC assumes that correct energies are measured by PMTs. Thus, the event selection efficiency taken from MC is same for "No LEC" and "LEC 140" as both have the same number of simulated events in the final states. The difference in "No LEC" and "LEC 140" comes from the different number of the real events in the data.

Use of LEC Flag

The LEC flag (Sec. 2.4.3) is also tested. As shown in Fig 5.4 most of the events have LEC flag = 0 while some have flag = 2. Also a small portion of events is associated with bad PMTs with flag ≥ 8. Therefore, the following selection criteria are applied as well as the cuts on the LEC value.

- No cuts on LEC flag.
- Flag = 0
- Flag ≤ 2

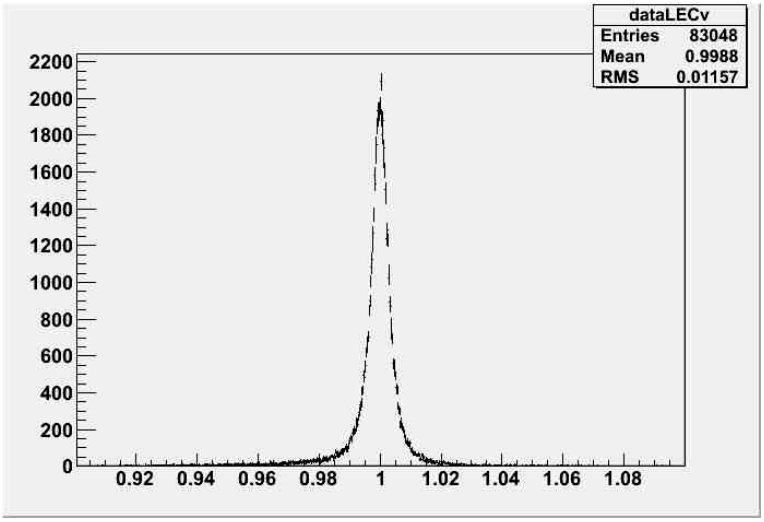

Figure 5.3: The distribution of LEC values for the two electron channel.

- Flag ≤ 8

The different criteria are applied to Phase 2 data and the foil geometry described in Sec. 2.2.1 is used. The qualities of fit are evaluated by comparing χ^2 value of each plots.

As shown in Fig. 5.5, nearly half of the data is not used for "Flag = 0" comparing to the "No Flag cut" (Fig. 5.8). The "Flag $\leq$ 2" (Fig. 5.6) has about the same order of statistics and the quality of fit to the "Flag $\leq$ 8" (Fig. 5.7). But "Flag $\leq$ 8" includes the events with the amplitude of LEC value $>$ 5 %, i.e. very unstable PMTs. Hence it is less reliable than the "Flag $\leq$ 2". Therefore, "Flag $\leq$ 2" requirement is used in the final analysis. In general, LEC 140 has slightly more statistics than LEC 00 while LEC 00 has much smaller χ^2 value than LEC 140 and No LEC. LEC 140 has more events than No LEC. It implies that there are more events that are increased their energy than the events that are decreased their energy in the low energy

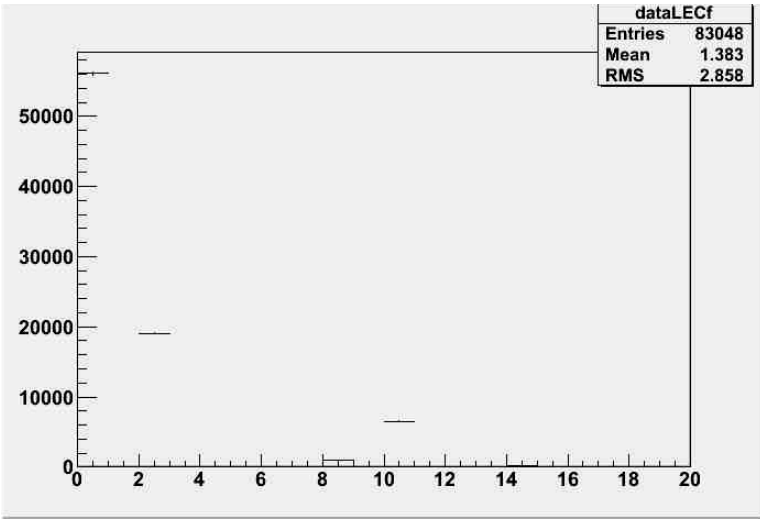

Figure 5.4: The distribution of LEC flags for the 2 electron channel.

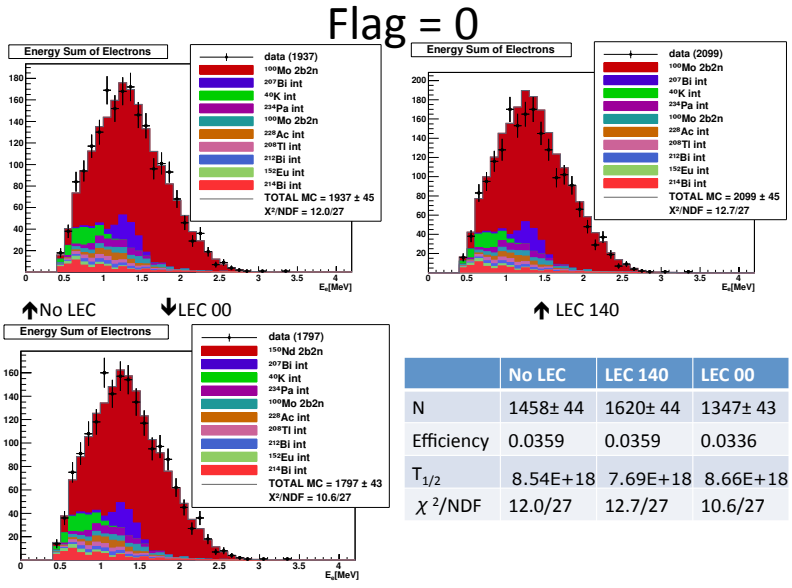

	No LEC	LEC 140	LEC 00
N	1458± 44	1620± 44	1347± 43
Efficiency	0.0359	0.0359	0.0336
$T_{1/2}$	8.54E+18	7.69E+18	8.66E+18
χ^2/NDF	12.0/27	12.7/27	10.6/27

Figure 5.5: Three different use of LEC value for LEC flag = 0.

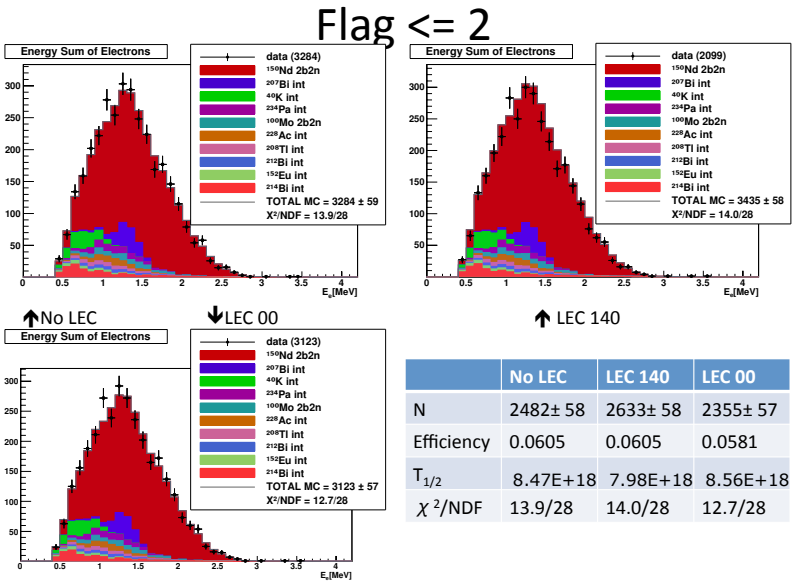

	No LEC	LEC 140	LEC 00
N	2482± 58	2633± 58	2355± 57
Efficiency	0.0605	0.0605	0.0581
$T_{1/2}$	8.47E+18	7.98E+18	8.56E+18
χ^2/NDF	13.9/28	14.0/28	12.7/28

Figure 5.6: Three different use of LEC value for LEC flag ≤ 2.

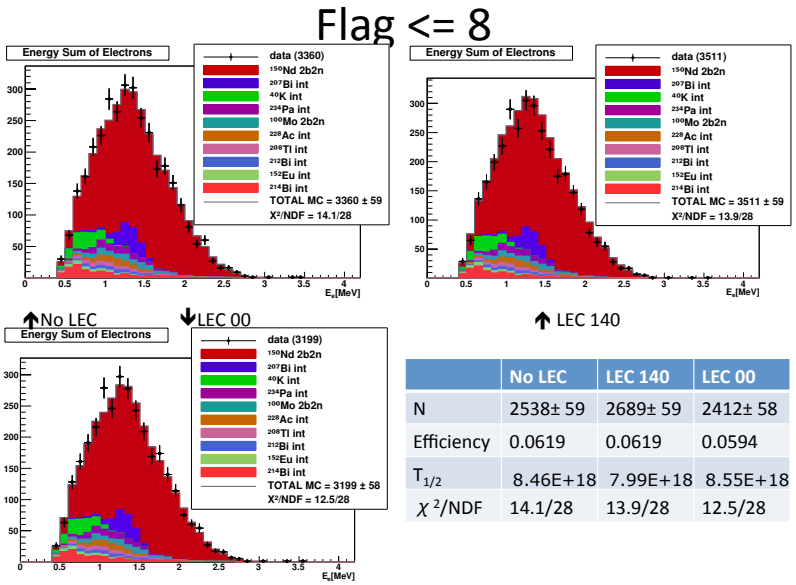

	No LEC	LEC 140	LEC 00
N	2538± 59	2689± 59	2412± 58
Efficiency	0.0619	0.0619	0.0594
$T_{1/2}$	8.46E+18	7.99E+18	8.55E+18
χ^2/NDF	14.1/28	13.9/28	12.5/28

Figure 5.7: Three different use of LEC value for LEC flag ≤ 8.

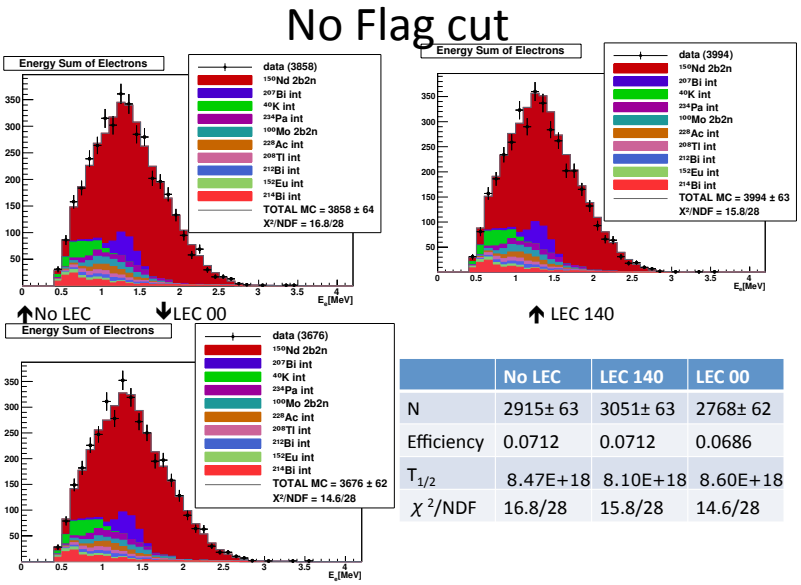

	No LEC	LEC 140	LEC 00
N	2915± 63	3051± 63	2768± 62
Efficiency	0.0712	0.0712	0.0686
$T_{1/2}$	8.47E+18	8.10E+18	8.60E+18
χ^2/NDF	16.8/28	15.8/28	14.6/28

Figure 5.8: Three different use of LEC value for no LEC flag cut.

region so that more events passed through the > 2 MeV requirements. As they are expected to have similar results, it is found that many uncorrected events are expected to be corrected to lower energy. Therefore LEC 00 is found to describe the data better than other uses of LEC value. Hence LEC 00 is used as a part of event selection criteria.

5.3 $2\nu\beta\beta$ Half-life

After the event selection described above including the change in the foil geometry and the application of LEC, the selection efficiency for ^{150}Nd is found to be 5.42 % and 5.77 % for Phase 1 and Phase 2, respectively. ^{150}Nd MC is fit to the background-subtracted data and 671.6 $\pm$ 31.1 events and 2234.2 $\pm$ 55.9 events are expected to fit for Phase 1 data and Phase 2 data, re-

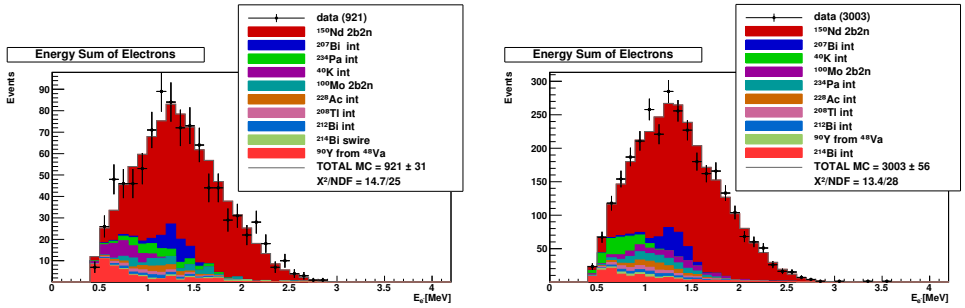

(a)

(b)

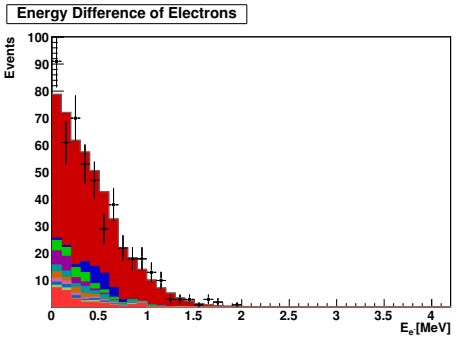

(c)

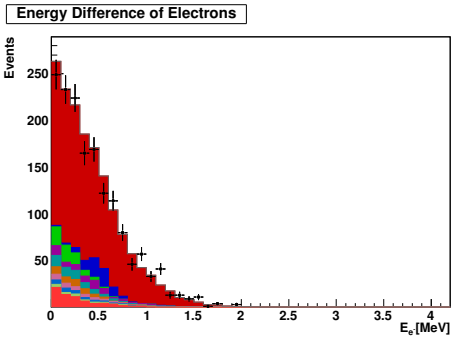

(d)

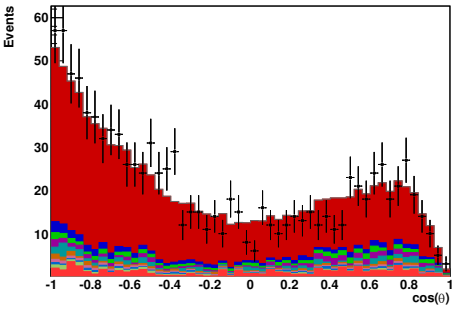

(e)

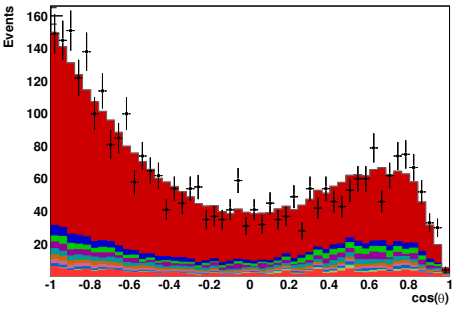

(f)

Figure 5.9: (a, b) energy sum of two electrons; (c, d) energy difference of two electrons; (e, f) cosine of the angle between two electrons. (a, c, e) Phase 1 data and they are described by the legend in (a); (b, d, f) Phase 2 data and they are described by the data in (b).

spectively. The energy difference between two electrons is also described well with χ^2/NDF value less than 1 for both Phase 1 and 2. Fig. 5.9 (a, b, c, d) shows that the energy spectrum of the data is described by MCs well with corresponding χ^2/NDF of the energy sum plots of 14.7/25 for Phase 1 and 13.4/28 for Phase 2. From Fig. 5.9, the number of decayed ^{150}Nd atoms,

$$N_{decayed}(t) = \frac{N(t)}{\varepsilon}, \tag{5.4}$$

is found to be

$$N_{decayed}(\text{Phase1}) = 12384 \pm 573 \text{ (stat)} \tag{5.5}$$

and

$$N_{decayed}(\text{Phase2}) = 38721 \pm 969 \text{ (stat)}. \tag{5.6}$$

Therefore,

$$N_{decayed}(\text{Phase1} + 2) = 51105 \pm 1541 \text{ (stat)}. \tag{5.7}$$

Using Eq. 5.2, $T^{2\nu}_{1/2}$ was calculated to be

$$T^{2\nu}_{1/2} = \left(8.95^{+0.28}_{-0.26}(\text{stat})\right) \times 10^{18} \text{ years}. \tag{5.8}$$

The data of cosine of the angle between two electrons also agrees well with MCs with corresponding χ^2/NDF of 22.9/50 and 43.4/50 for Phase 1 and Phase 2, respectively. It suggests that the $V + A$ weak boson is strongly suppressed.

5.4 Systematic Uncertainties

The systematic uncertainties are introduced by the followings:

- Uncertainty in LEC. The results are compared with the one which both LEC flag and value are not applied and the uncertainty in 2 electron analysis is found to be 0.6% by calculating the deviation.

- Uncertainty in the background model. Using the background model that is shifted by an amount of one systematic uncertainties gained in Chap. 4, the MCs are re-fitted to the data. As a result, the uncertainty induced in 2 electron analysis is found to be 0.9%.

- Uncertainty due to the two different Rn background model. In the background model used in this dissertation, there are separate MCs for Rn sitting on the surface of the foil, on the surface of the tracking wires and contaminated in the foil. However, there is a different background model that approximates Rn background events only by the MC of Rn sitting on the surface of the wires [25]. Fig. 5.10 shows the plots of energy sum with "Triple components model" and "Single components model" and the deviation of 0.8 % is found as shown in Tab. 5.1.

- Uncertainty in the tracking algorithm. Two tracking algorithms are developed for NEMO-3. However they are found to have a difference of 5.4% in the resultant event selections [26].

By calculating a quadratic sum of the contributions to the uncertainties, a total of 5.6% of systematic uncertainty is estimated.

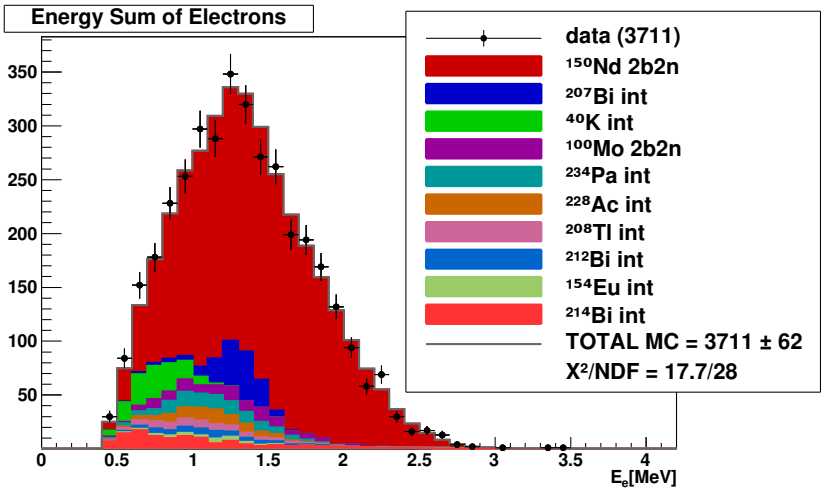

(a)

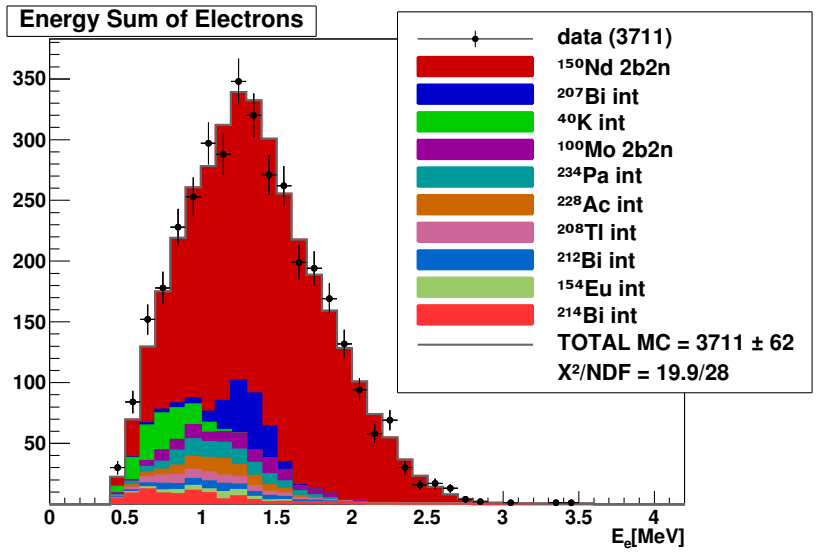

(b)

Figure 5.10: Energy sum of 2 electron events of Phase 2 data with (a) "Triple components model" and (b) "Single components model" of Rn background.

	No. of Events	
	Triple components model	Single components model
^{150}Nd $2\nu\beta\beta$	2815±60	2838±60
Background MC	896±82	873±81
Total Mc	3711±62	
Data	3711	

Table 5.1: Details of the fit for Fig 5.10.

5.5 Summary and Discussion

To improve the analysis, the foil geometry is optimized and the use of LEC is investigated. This yield that $2\nu\beta\beta$ half-life of ^{150}Nd is determined to be

$$T^{2\nu}_{1/2} = \left(8.95^{+0.28}_{-0.26}(\text{stat}) \pm 0.50(\text{sys})\right) \times 10^{18} \text{ years} \tag{5.9}$$

This agrees with the previous result

$$T^{2\nu}_{1/2} = \left(9.11^{+0.25}_{-0.22}(\text{stat}) \pm 0.62(\text{sys})\right) \times 10^{18} \text{ years} \tag{5.10}$$

within one standard deviation [15]. The systematic uncertainty in the energy measurement was reduced from 1 % to 0.6 % by introducing LEC. Also the uncertainty in the foil geometry, which was found to be 3 % in the previous analysis is removed because the bug in MC production was fixed.

Chapter 6

Conclusions

In this dissertation, a precise measurement of the $2\nu\beta\beta$ half-life of ^{150}Nd including a construction of the background model is presented. The activities of the internal background are studied with the one electron plus one photon, one electron plus two photons and one electron channels. The results are summarized in Tab. 4.1. The external background model is also validated with the one electron plus one photon channel. In the two electron channel, the boundaries between the ^{150}Nd foil and the adjacent foils are adjusted to maximize the yield of the signal. The use of LEC was investigated and it was found that applying an LEC value and rejecting the events with LEC flag > 2 improves the results. The $2\nu\beta\beta$ half-life is obtained to be

$$T_{1/2}^{2\nu} = \left(8.95^{+0.28}_{-0.26}(\text{stat}) \pm 0.50(\text{sys})\right) \times 10^{18} \text{ years}, \tag{6.1}$$

which agrees with the previous analysis within one standard deviation. Due to the introduction of LEC flag cuts, the statistical uncertainty increased slightly. However, the systematic uncertainty was reduced because of the use of LEC. The systematic uncertainty is dominated by the uncertainty in the tracking algorithm and could be improved in the future. As $2\nu\beta\beta$ de-

cay is an irreducible background for $0\nu\beta\beta$ decay, the result is important for $0\nu\beta\beta$ search and and the systematic uncertainty needs to be reduced since the statistics of $0\nu\beta\beta$ is low.

Appendix A

Details of Activity Measurements

The details of the fits for Fig. 4.5, 4.6, 4.7, 4.9, 4.10, 4.11, 5.5, 5.6, 5.7, 5.8 and 5.9 are provided in this chapter.

Isotope	No. of Events	Activity (Bq)
^{208}Tl int	80.13±9.4	$(6.10\pm0.71)\times10^{-4}$
^{214}Bi swire	3.73±0.58	1.20
^{214}Bi int	2.29±0.19	1.87×10^{-4}
^{208}Tl from ^{9}6Zr	0.32±0.00	9.10×10^{-5}
^{208}Tl pmt	0.22±0.16	27.0
^{208}Tl exbg7	0.17±0.17	3.07
^{208}Tl from ^{100}Mo	0.0966±0.0216	1.15×10^{-4}
^{214}Bi from ^{96}Zr	0.0791±0.0250	1.90×10^{-4}
^{214}Bi from ^{100}Mo	0.0210±0.0210	5.00×10^{-5}
^{214}Bi from ^{48}Ca	$(1.86\pm0.83)\times10^{-3}$	4.45×10^{-6}
Total MC	87±9	
Data	87	

Table A.1: Details of the fit for Fig 4.5 (a), (c) and (e).

Isotope	No. of Events	Activity (Bq)
^{208}Tl int	245±20	$(6.07\pm0.40)\times10^{-4}$
^{214}Bi int	5.97±0.30	1.87×10^{-4}
^{214}Bi swire	3.12±0.23	0.198
^{208}Tl from ^{9}6Zr	1.09±0.10	9.10×10^{-5}
^{208}Tl pmt	1.01±0.34	27.0
^{208}Tl exbg7	0.85±0.38	3.07
^{214}Bi pmt	0.49±0.49	324
^{208}Tl exbg4	0.401±0.40	484
^{208}Tl from ^{100}Mo	0.25±0.00	1.15×10^{-4}
^{214}Bi from ^{96}Zr	0.17±0.00	1.90×10^{-4}
Total Mc	258±16	
Data	258	

Table A.2: Details of the fit for Fig 4.5 (b), (d) and (f).

Isotope	No. of Events	Activity (Bq)
^{207}Bi int	1091±47	(1.17±0.05)×10^{-2}
^{208}Tl int	118±7	6.10×10^{-4}
^{228}Ac int	90.7±2.3	1.69×10^{-3}
^{214}Bi exbg2	66.0±9.4	566.5
^{214}Bi swire	51.6±2.1	1.20
^{214}Bi exbg4	50.0±6.6	7360
^{214}Bi pmt	49.1±4.9	324
^{40}K pmt	38.2±6.0	1080
^{212}Bi int	30.3±1.3	1.69×10^{-3}
^{214}Bi int	25.8±0.6	1.87×10^{-4}
Others	154 ±19	
Total Mc	1683±46	
Data	1683	

Table A.3: Details of the fit for Fig 4.6 (a), (c) and (e).

Isotope	No. of Events	Activity (Bq)
^{207}Bi int	3055±56	(1.10±0.02)×10^{-2}
^{208}Tl int	353±18	6.07×10^{-4}
^{228}Ac int	255±13	1.69×10^{-3}
^{214}Bi exbg4	131±10	7.36×10^{3}
^{214}Bi pmt	130±10	324
^{40}K pmt	109±10	1080
^{212}Bi int	91.54±2.3	1.69×10^{-3}
^{214}Bi int	78.31±1.1	1.87×10^{-4}
^{40}K exbg7	33.1±3.0	100
^{234m}Pa int	31.0±1.4	1.82×10^{-3}
Others	160 ±34	
Total Mc	4426±72	
Data	4426	

Table A.4: Details of the fit for Fig 4.6 (b), (d) and (f).

Isotope	No. of Events	Activity (Bq)
^{207}Bi int	1656±66	1.17×10^{-2}
^{228}Ac int	1167±58	1.69×10^{-3}
^{208}Tl int	664±33	6.10×10^{-4}
^{214}Bi swire	454±10	1.20
^{214}Bi exbg2	366±20	566
^{214}Bi exbg2	318±20	7360
^{214}Bi pmt	288±10	324
^{152}Eu int	270±20	$(2.06\pm0.15)\times10^{-3}$
^{214}Bi int	206±0.0	1.87×10^{-4}
^{212}Bi int	159±0.3	1.69×10^{-3}
Others	1003±10	
Total Mc	6711±47	
Data	6605	

Table A.5: Details of the fit for Fig 4.7 (a), (c) and (e).

Isotope	No. of Events	Activity (Bq)
^{207}Bi int	4627±93	1.10×10^{-2}
^{228}Ac int	3480±82	1.69×10^{-3}
^{208}Tl int	2007±60	6.07×10^{-4}
^{214}Bi exbg4	868±30	7360
^{214}Bi pmt	850±20	324
^{152}Eu int	736±40	$(1.88\pm0.10)\times10^{-3}$
^{154}Eu int	625±30	$(9.35\pm0.50)\times10^{-4}$
^{214}Bi int	612±0.0	1.87×10^{-4}
^{40}K pmt	486±20	1.08×10^{3}
^{212}Bi int	479±0.1	1.69×10^{-3}
Others	2528 ±24	
Total Mc	17298±72	
Data	17221	

Table A.6: Details of the fit for Fig 4.7 (b), (d) and (f).

Isotope	No. of Events	Activity (Bq)
^{208}Tl int	30.72±0.2	$(5.00\pm0.90)\times10^{-4}$
^{208}Tl from ^{96}Zr	0.15±0.0	9.10×10^{-5}
^{214}Bi swire	0.0748±0.0748	1.20
^{208}Tl from ^{100}Mo	0.0384±0.0136	1.15×10^{-4}
^{214}Bi int	0.0283±0.0200	1.70×10^{-4}
^{208}Tl from ^{48}Ca	0.0114±0.0022	5.25×10^{-6}
^{214}Bi from ^{48}Ca	$(3.72\pm3.71)\times10^{-4}$	4.45×10^{-6}
Total Mc	31±0.0	
Data	31	

Table A.7: Details of the fit for Fig 4.9 (a), (c) and (e).

Isotope	No. of Events	Activity (Bq)
^{208}Tl int	119±0.0	$(6.60\pm0.06)\times10^{-4}$
^{208}Tl from ^{96}Zr	0.65±0.0	9.10×10^{-5}
^{208}Tl from ^{100}Mo	0.11±0.0	1.15×10^{-4}
^{214}Bi int	0.0989±0.0374	1.70×10^{-4}
^{214}Bi swire	0.0610±0.0306	0.198
^{208}Tl from ^{48}Ca	0.0236±0.0032	5.25×10^{-6}
Total Mc	120±0.0	
Data	120	

Table A.8: Details of the fit for Fig 4.9 (b), (d) and (f).

Isotope	No. of Events	Activity (Bq)
^{40}K int	(6.64±0.05)×10^{4}	(1.03±0.01)×10^{-2}
^{210}Bi sfoil	(2.58±0.05)×10^{4}	1.87±0.04
^{210}Bi swire	(2.51±0.03)×10^{4}	9.93
^{234m}Pa int	(1.88±0.04)×10^{4}	(2.07±0.03)×10^{-3}
^{212}Bi int	(9.39±0.02)×10^{3}	1.84×10^{-3}
^{90}Y from ^{48}Ca	(5.66±0.00)×10^{3}	3.00×10^{-2}
^{228}Ac int	(3.44±0.01)×10^{3}	1.84×10^{-3}
^{40}K from ^{96}Zr	(3.25±0.00)×10^{3}	1.97×10^{-2}
^{207}Bi int	(2.83±0.01)×10^{3}	1.12×10^{-2}
^{214}Bi swire	(2.76±0.00)×10^{3}	1.20
Others	11388 ±110	
Total Mc	174780±220	
Data	1744773	

Table A.9: Details of the fit for Fig 4.10 (a) and (c).

Isotope	No. of Events	Activity (Bq)
^{40}K int	(2.02±0.01)×10^{5}	(1.02±0.01)×10^{-2}
^{210}Bi swire	(7.11±0.00)×10^{4}	8.92
^{210}Bi sfoil	(6.65±0.02)×10^{4}	1.59±0.02
^{234m}Pa int	(5.11±0.04)×10^{4}	(1.85±0.02)×10^{-3}
^{212}Bi int	(2.86±0.02)×10^{4}	1.84×10^{-3}
^{90}Y from ^{48}Ca	(1.68±0.00)×10^{4}	3.00×10^{-2}
^{228}Ac int	(1.06±0.01)×10^{4}	1.84×10^{-3}
^{40}K from ^{96}Zr	(9.62±0.00)×10^{3}	1.97×10^{-2}
^{207}Bi int	(8.87±0.02)×10^{3}	1.12×10^{-2}
^{150}Nd $2\nu\beta\beta$	(4.26±0.09)×10^{3}	3.70×10^{-4}
Others	27919 ±250	
Total Mc	497000±290	
Data	496999	

Table A.10: Details of the fit for Fig 4.10 (b) and (d).

Isotope	No. of Events	Activity (Bq)
^{214}Bi exbg2	403±20	566
^{214}Bi pmt	375±10	324
^{214}Bi exbg4l	233±10	7360
^{40}K pmt	202±10	1080
^{208}Tl pmt	62.3±2.6	27.0
^{60}Co exbg8	57.5±3.1	23.3
^{208}Tl exbg4	52.4±4.6	484
^{60}Co exbg17	51.3±7.9	76.1
^{234m}Pa exbg8	50.0±6.7	3420
^{60}Co exbg6	48.4±5.6	29.4
Others	217 ±13	
Total Mc	1702±37	
Data	1255	

Table A.11: Details of the fit for Fig 4.11 (a) and (c).

Isotope	No. of Events	Activity (Bq)
^{214}Bi pmt	1114±30	324
^{214}Bi exbg4	736±30	7360
^{40}K pmt	554±20	1080
^{208}Tl pmt	189±10	27.0
^{234m}Pa exbg8	158±10	3420
^{208}Tl exbg4	145±10	484
^{228}Ac pmt	142±10	72.7
^{60}Co exbg17	111±10	47.6
^{60}Co exbg8	107±10	14.6
^{60}Co exbg6	89.5±6.0	18.4
Others	473 ±23	
Total Mc	3817±53	
Data	2717	

Table A.12: Details of the fit for Fig 4.11 (b) and (d).

	No. of Events		
Isotope	No LEC	LEC140	LEC00
^{150}Nd $2\nu\beta\beta$	1458±44	1620±44	1348±43
^{207}Bi int	90.6±1.9	90.6±1.9	84.9±1.8
^{40}K int	71.8±2.5	71.8±2.5	67.3±2.4
^{234m}Pa int	60.1±1.9	60.1±1.9	56.9±1.8
^{100}Mo $2\nu\beta\beta$	55.1±4.2	55.1±4.2	49.9±4.0
^{228}Ac int	43.9±1.6	43.9±1.6	41.0±1.6
^{208}Tl int	36.8±0.2	36.8±0.2	34.5±0.2
^{212}Bi int	29.7±1.4	29.7±1.4	27.9±1.3
^{152}Eu int	19.3±0.8	19.3±0.8	18.3±0.8
^{214}Bi int	11.8±0.4	11.8±0.4	11.2±0.4
Others	60.0±7.8	60.0±7.8	57.3±5.0
Total Mc	1937±45	2099±45	1797±43
Data	1937	2099	1797

Table A.13: Details of the fit for Fig 5.5.

	No. of Events		
Isotope	No LEC	LEC140	LEC00
^{150}Nd $2\nu\beta\beta$	2482±58	2633±58	2355±57
^{207}Bi int	149±4	149±4	143±3
^{40}K int	121±4	121±4	117±3
^{234m}Pa int	96.9±2.4	96.9±2.4	93.5±2.3
^{100}Mo $2\nu\beta\beta$	96.5±5.6	96.5±5.6	91.0±5.4
^{228}Ac int	74.1±2.1	74.1±2.1	70.9±2.1
^{208}Tl int	61.8±0.3	61.8±0.3	59.3±0.3
^{212}Bi int	46.7±1.7	46.7±1.7	44.8±1.7
^{152}Eu int	33.2±1.1	33.2±1.1	32.0±1.0
^{214}Bi int	19.3±0.5	19.3±0.5	18.7±0.5
Others	103±10	103±10	97.0±9.2
Total Mc	3284±59	3435±58	3123±57
Data	3284	3435	3123

Table A.14: Details of the fit for Fig 5.6.

	No. of Events		
Isotope	No LEC	LEC140	LEC00
^{150}Nd $2\nu\beta\beta$	2538±59	2689±59	2412±58
^{207}Bi int	153±5	153±5	147±3
^{40}K int	123±4	123±4	119±3
^{234m}Pa int	98.8±2.4	98.8±2.4	95.5±2.4
^{100}Mo $2\nu\beta\beta$	98.5±5.6	98.5±5.6	93.0±5.5
^{228}Ac int	76.1±2.2	76.1±2.2	72.9±2.1
^{208}Tl int	63.1±0.3	63.1±0.3	60.6±0.3
^{212}Bi int	48.2±1.7	48.2±1.7	46.2±1.7
^{152}Eu int	33.9±1.1	33.9±1.1	32.7±1.0
^{214}Bi int	19.7±0.6	19.7±0.6	19.0±0.5
Others	107±10	107±10	102±10
Total Mc	3360±59	3511±59	3199±58
Data	3360	3511	3123

Table A.15: Details of the fit for Fig 5.7.

	No. of Events		
Isotope	No LEC	LEC140	LEC00
^{150}Nd $2\nu\beta\beta$	2915±63	3051±63	2768±62
^{207}Bi int	175±5	175±5	168±3
^{40}K int	140±5	140±5	135±3
^{100}Mo $2\nu\beta\beta$	117±7.2	117±7.2	111±5.5
^{234m}Pa int	116±3.4	116±3.4	113±2.4
^{228}Ac int	87.1±2.3	87.1±2.3	83.8±2.3
^{208}Tl int	72.6±0.3	72.6±0.3	70.0±0.3
^{212}Bi int	54.7±1.8	54.7±1.8	52.6±1.8
^{152}Eu int	39.0±1.1	39.0±1.1	37.8±1.2
^{214}Bi int	22.3±0.6	22.3±0.6	21.6±0.6
Others	120±11	120±11	116±11
Total Mc	3858±64	3994±63	3676±62
Data	3858	3994	3676

Table A.16: Details of the fit for Fig 5.8.

Isotope	No. of Events	Activity (mBq)
^{150}Nd $2\nu\beta\beta$	672±53	0.361±0.017
^{207}Bi int	42.7±1.3	11.9
^{234m}Pa int	34.7±1.5	20.7
^{40}K int	32.4±1.7	10.3
^{100}Mo $2\nu\beta\beta$	32.1±3.2	7.80
^{228}Ac int	17.5±0.9	1.54
^{208}Tl int	14.0±0.1	0.55
^{212}Bi int	12.0±0.8	1.54
^{214}Bi swire	10.3±0.9	120×10^3
^{90}Y from ^{48}Ca	6.98±1.32	30.0
Others	46.3 ±3.6	
Total Mc	921±31	
Data	921	

Table A.17: Details of the fit for Fig 5.9 (a), (c) and (e).

Isotope	No. of Events	Activity (mBq)
^{150}Nd $2\nu\beta\beta$	2234±56	0.358±0.010
^{207}Bi int	136±3	10.9
^{40}K int	116±2	10.2
^{100}Mo $2\nu\beta\beta$	104±11	7.80
^{234m}Pa int	99.2±2.5	1.85
^{228}Ac int	65.9±2.0	1.76
^{208}Tl int	55.4±0.2	0.63
^{212}Bi int	42.20±1.6	1.76
^{90}Y from ^{48}Ca	25.4±2.5	30.0
^{214}Bi int	18.5±0.5	0.187
Others	80.8±5.4	
Total Mc	3003±56	
Data	3003	

Table A.18: Details of the fit for Fig 5.9 (b), (d) and (f).

References

[1] L.M. Brown. The idea of the neutrino. *Phys. Today*, 31:23, 1978.

[2] E. Fermi. An attempt of a theory of beta radiation. 1. *Z.Phys.*, 88:161–177, 1934.

[3] K. Abe et al. Indication of Electron Neutrino Appearance from an Accelerator-produced Off-axis Muon Neutrino Beam. *Phys. Rev. Lett.*, 107:041801, 2011.

[4] R. Arnold, C. Augier, A.M. Bakalyarov, J. Baker, A. Barabash, et al. Technical design and performance of the NEMO 3 detector. *Nucl.Instrum.Meth.*, A536:79–122, 2005.

[5] B. T. Cleveland et al. Measurement of the solar electron neutrino flux with the Homestake chlorine detector. *Astrophys. J.*, 496:505–526, 1998.

[6] Ping Yang and Qiu-Yu Liu. Solar Neutrino Oscillation Parameters after SNO Phase-III and SAGE Part-III. *Chin. Phys. Lett.*, 26:081402, 2009.

[7] K. Abe et al. Solar neutrino results in Super-Kamiokande-III. *Phys. Rev.Lett.*, D83:052010, 2011.

[8] Alain Bellerive. Review of solar neutrino experiments. *Int. J. Mod. Phys.*, A19:1167–1179, 2004.

[9] M. C. Gonzalez-Garcia and M. Maltoni. Status of Oscillation plus Decay of Atmospheric and Long- Baseline Neutrinos. *Phys. Lett.*, B663:405–409, 2008.

[10] P. Adamson et al. Search for muon-neutrino to electron-neutrino transitions in MINOS. *Phys. Rev. Lett.*, 103:261802, 2009.

[11] S.J. Freeman. Constraining nuclear matrix elements for neutrinoless double beta decay. NEMO-3 internal note, 2011.

[12] V. Tretyak. The nemo3 results after completion of the data taking. MEDEX 2011, 2011.

[13] R. Arnold et al. Technical performance of the NEMO 3 detector "Advantages and limitations". Technical report, 2005. Corinne AUGIER for the NEMO Collaboration.

[14] K. Chaturvedi, R. Chandra, P. K. Rath, P. K. Raina, and J. G. Hirsch. Nuclear deformation and neutrinoless double-β decay of ^{94,96}Zr, ^{98,100}Mo, ^{104}Ru, ^{110}Pd, ^{128,130}Te and ^{150}Nd nuclei in mass mechanism. *Phys. Rev. Lett.*, C78:054302, 2008.

[15] Nasim Fatemi-Ghomi. *Measurement of the double beta decay half-life of Nd-150 and search for neutrinoless decay modes with NEMO-3 detector.* PhD thesis, University of Manchester, 2009.

[16] V. Tretyak. Laser energy corrections for the year 2010. NEMO-3 internal note, June 2011.

[17] V. Kovalenko. Laser time corrections (ltcs) for the nemo3 data. NEMO-3 internal note, 2006.

[18] O. A. Ponkratenko, V. I. Tretyak, and Yu. G. Zdesenko. The Event generator DECAY4 for simulation of double beta processes and decay of radioactive nuclei. *Phys. Atom. Nucl.*, 63:1282–1287, 2000.

[19] R. Brun, F. Bruyant, M. Maire, A. C. McPherson, and P. Zanarini. GEANT3. 1987. CERN-DD-EE-84-1.

[20] V. Vasiliev and B. Pahlka. rootana documentation and users guide. NEMO-3 internal note, 2009.

[21] Rene Brun, Philippe Canal, and Fons Rademakers. Design, development and evolution of the ROOT system. *PoS*, ACAT2010:002, 2010.

[22] L. Le Cam. Maximum likelihood: An introduction. *International Statistical Review / Revue Internationale de Statistique*, 58(2):pp. 153–171, 1990.

[23] J. Argyriades et al. Measurement of the background in the NEMO 3 double beta decay experiment. *Nucl. Instrum. Meth.*, A606:449–465, 2009.

[24] Chris M. Jackson. *Double Beta Decay of 150Nd in NEMO-III and Studies Towards the Design of SuperNEMO.* PhD thesis, University of Manchester, 2010.

[25] V. Kovalenko. Radon level estimation. NEMO-3 internal note, March 2007.

[26] F. Nova. comparison of events ucl/vera. NEMO-3 internal note, July 2011.